Mon. Not. R. Astron. Soc. **000**, 1–19 (2013) Printed 21 August 2014 (MN LATEX style file v2.2)

# Modeling the [Fe II]$\lambda$1.644$\mu$m outflow and comparison with $H_2$ and $H^+$ kinematics in the inner 200 pc of NGC 1068

F. K. B. Barbosa[1⋆], T. Storchi-Bergmann[2], P. McGregor[3] and T. B. Vale[4]
[1] *IFRS – Campus Restinga, Rua 7121, n. 285 Lote 16, Quadra F, Restinga, CEP 91791-508, Porto Alegre, RS, Brazil*
[2] *Instituto de Física – UFRGS, Caixa Postal 15051, CEP 91501-970, Porto Alegre, RS, Brazil*
[3] *Research School of Astronomy and Astrophysics, Australian National University, Cotter Road, Weston Creek, ACT 2611, Australia*
[4] *INFES – UFF, Rua João Jasbick, s/n, Bairro Aeroporto, CEP 28470-000 Santo Antônio de Pádua, RJ, Brazil*

arXiv:1408.4750v1 [astro-ph.GA] 20 Aug 2014

Accepted 2012 April 15. Received 2012 February 14; in original form 2012 February 11

**ABSTRACT**

We map the kinematics of the inner (200 pc) narrow-line region (NLR) of the Seyfert 2 galaxy NGC 1068 using the instrument NIFS and adaptative optics at the Gemini North Telescope. Channel maps and position-velocity diagrams are presented at a spatial resolution of $\cong 10$ pc and spectral resolution $\sim 5300$ in the emission lines [Fe II] $\lambda\,1.644\,\mu$m, $H_2\,\lambda\,2.122\,\mu$m and Br$\gamma$. The [Fe II] emission line provides a better coverage of the NLR outflow than the previously used [O III] $\lambda\,5007$ emission line, extending beyond the area of the bi-polar cone observed in Br$\gamma$ and [O III]. This is mainly due to the contribution of the redshifted channels to the NE of the nucleus, supporting its origin in a partial ionized zone with additional contribution from shocks of the outflowing gas with the galactic disc. We modeled the kinematics and geometry of the [Fe II] emitting gas finding good agreement with the data for outflow models with conical and lemniscate (or hourglass) geometry. We calculate a mass outflow rate of $1.9^{+1.9}_{-0.7}\,M_\odot\,yr^{-1}$ but a power for the outflow of only 0.08% $L_{Bol}$. The molecular ($H_2$) gas kinematics is completely distinct from that of [Fe II] and Br$\gamma$, showing radial expansion in an off-centered $\sim 100$ pc radius ring in the galaxy plane. The expansion velocity decelerates from $\approx 200\,km\,s^{-1}$ in the inner border of the ring to approximately zero at the outer border where our previous studies found a 10 Myr stellar population.

**Key words:** galaxies: individual: NGC 1068 – galaxies: active – galaxies: kinematics and dynamics – galaxies: nuclei – galaxies: ISM – ISM: jets and outflows

## 1 INTRODUCTION

The kinematics of the narrow line region (NLR) of NGC 1068 has been the subject of many studies over the years, the most recent and detailed being those of Cecil et al. (2002) and Das et al. (2006), based on long-slit optical spectroscopy of the inner few hundred parsecs obtained with the Space Telescope Imaging Spectrograph aboard the Hubble Space Telescope (*HST-STIS*). Das et al. (2006) have shown that the NLR gas is outflowing in a hollow bi-cone, along which the gas seems to be accelerated up to 140 pc from the nucleus and then decelerated.

Integral field optical spectroscopy of the inner 1.5 kpc was obtained by Emsellem et al. (2006) using the instrument SAURON – at lower spatial resolution but covering a larger region of the galaxy than in Das et al. (2006). Emsellem et al. (2006) observed the outflow in [O III] $\lambda\,5007$ and H$\beta$, finding also streaming motions towards the nucleus and emission knots of H$\beta$ attributed to regions of star formation in the galaxy plane. Gerssen et al. (2006) presented optical integral field observations of the inner 400 pc using the Gemini Multi-Object Spectrograph Integral Field Unit (GMOS-IFU) at a better spatial resolution ($\approx 40$ pc) which revealed, besides high-velocity gas emission from outflowing gas, also some emission from the gas in the galaxy disc.

In the near-infrared (hereafter near-IR), Müller Sánchez et al. (2009) and Müller-Sánchez et al. (2011) have mapped the gas kinematics via integral field observations using the instrument SINFONI at the Very Large Telescope (VLT). While Müller Sánchez et al. (2009) focus on the $H_2$ kinematics in the inner few tens of pc which revealed inflows, Müller-Sánchez et al. (2011) focus on the Br$\gamma$ and coronal lines kinematics, which are dominated by outflows.

In Riffel et al. (2013b) (hereafter Paper I) we have used the Gemini Near-infrared Integral Field Spectrograph (NIFS) on the Gemini North telescope operating with the

⋆ E-mail: fausto.barbosa@restinga.ifrs.edu.br

adaptive optics module ALTAIR to map the flux distributions and excitation of the gas within the inner 300 pc, while in Storchi-Bergmann et al. (2012) we have studied the stellar population.

In this paper, we present detailed measurements of the gas kinematics observed in the near-IR emission lines [Fe II] $\lambda\,1.644\,\mu$m, $H_2\,\lambda\,2.122\,\mu$m and Br$\gamma$ using channel maps and position velocity diagrams. We concluded this is the best way to separate the multiple kinematic components which are present in the emitting gas in this galaxy. The [Fe II] gas kinematics shows a "broader" outflow than previously observed in [O III] and in the near-IR coronal lines, being similar to that observed in planetary nebulae and consistent with an origin in an accretion disc wind (Proga & Kallman 2004) or a torus wind (Elvis 2000). We test three models with different geometries in order to reproduce the outflow.

Throughout this paper we adopt a distance of 14.4 Mpc to NGC 1068 which correspond to a scale of 72 pc arcsec$^{-1}$ at the galaxy. This paper is organized as follows. In Sec. 2 we present the observations, in Sec. 3 we discuss previous studies relevant to the present work, in Sec. 4 we present the gas kinematics (channel maps and *p-v* diagrams) , in Sec. 5 we give our interpretation to the kinematics of the [Fe II], Br$\gamma$ and $H_2$ , in Sec. 6 we perform the modeling and analysis, in Sec. 7 we calculate the mass outflow rate and corresponding power and in Sec. 8 we present our conclusions.

## 2 OBSERVATIONS AND DATA

The spectroscopic data was obtained at the Gemini North telescope, with NIFS (see McGregor et al. 2003), operating with the ALTAIR adaptive optics module. The data were obtained on the nights of November 26 and December 03 and 09, 2008, and in the present paper we have used spectra obtained in the H and K spectral bands at a resolving power of 5290.

NIFS has a square field of view of $3'' \times 3''$ and was set to a position angle of 300 degrees for the observations, resulting in a spatial sampling of 0.044 arcsec perpendicular to the jet (vertical direction in our images) and 0.103 arcsec along it (horizontal direction in our images). The angular resolution of the data, measured as the FWHM of the spatial profile of a star is $0\farcs11 \pm 0\farcs02$ at the H and K bands, corresponding to $\cong 8$ pc at the galaxy.

Dithering was applied in order to cover a field-of-view of $\cong 5'' \times 5''$. Additional details about the data can be found in Paper I .

## 3 PREVIOUS WORKS

On the basis of *HST-STIS* spectra, Das et al. (2006) proposed a kinematic model in which the NLR has the geometry of a hollow bicone oriented at PA of $30^\circ \pm 2$ as illustrated in Figure 1. This figure was adapted from their Figure 10 and rotated to the same orientation as our data. We have identified in this figure the line of nodes (LN), minor axis (MA) and cone axis (CA) as derived by Das et al. (2006). The walls of the cone – corresponding to the areas intersecting perpendicularly the plane of the sky – were also labeled

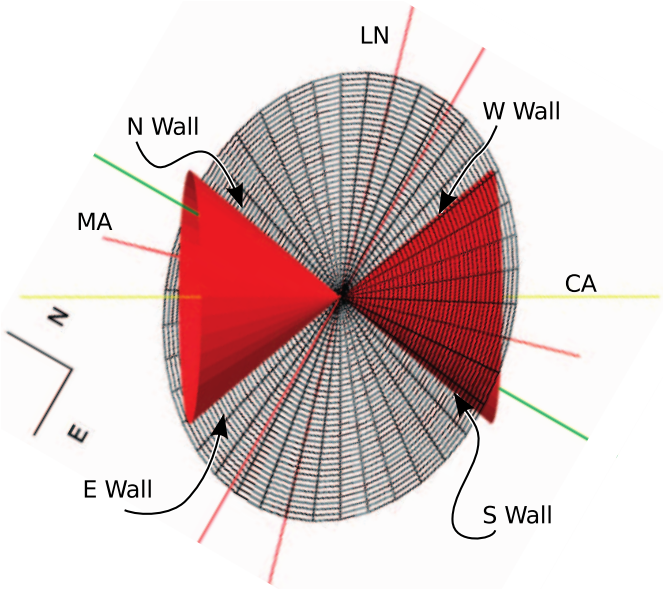


**Figure 1.** Geometry of the outflow relative to the galactic disc, adapted from Das et al. (2006), after a rotation to match the orientation of our data. The walls of the cone are labeled as N, E, S and W Walls. The labels LN, MA and CA correspond to the line of nodes, minor axis and cone axis, respectively.

in this figure as N, E, S and W Walls. The galactic plane is inclined by 40° such that the far side of the galaxy is the NE (de Vaucouleurs, G., et al. 1991). The NE side of the cone is in front of the galactic disc, while the SW side is behind and apparently obscured by the galactic disc. The bicone axis is tilted by 5° relative to the plane of the sky such that the NE side is oriented (slightly) toward us, while the SW side is oriented away from us. The cone is hollow but has "thick" walls, corresponding to inner and outer half-opening angles of 20° and 40°. The NLR gas flows away from the nucleus along the cone, reaching a maximum velocity of 2000 km s$^{-1}$ at 140 pc from the nucleus.

We present the integrated flux maps from Paper I in the lines [Fe II] $\lambda\,1.644\,\mu$m, Br$\gamma$ and $H_2\,\lambda\,2.122\,\mu$m, in Figures 2, 3 and 4, respectively. In Fig. 2 we identify the N, E, S and W walls of the bicone. In Fig. 3 the features indicated by arrows correspond to structures A, D, F and G previously identified in the [O III] map by Evans et al. (1991). In Fig. 4 the structures identified by Müller Sánchez et al. (2009) as *northern tongue* (NT) and *southern tongue* (ST) are also indicated by arrows. The main feature seen in the $H_2$ flux map is a ring which has its centre offset from the position of the nucleus by $0\farcs6$ to the SW (Müller Sánchez et al. 2009). We adopt as the position of the nucleus the location of the maximum of the K-band continuum emission.

## 4 GAS KINEMATICS

In a previous study, Mazzalay et al. (2013) has used the same NIFS data we used in the present paper to map the gas kinematics of the coronal line region, which is consistent with an origin of the emission in the inner part of the NLR. Here we present and discuss the kinematics of the low ionization lines of [Fe II] $\lambda\,1.644\,\mu$m, $H_2\,\lambda\,2.122\,\mu$m and Br$\gamma$,

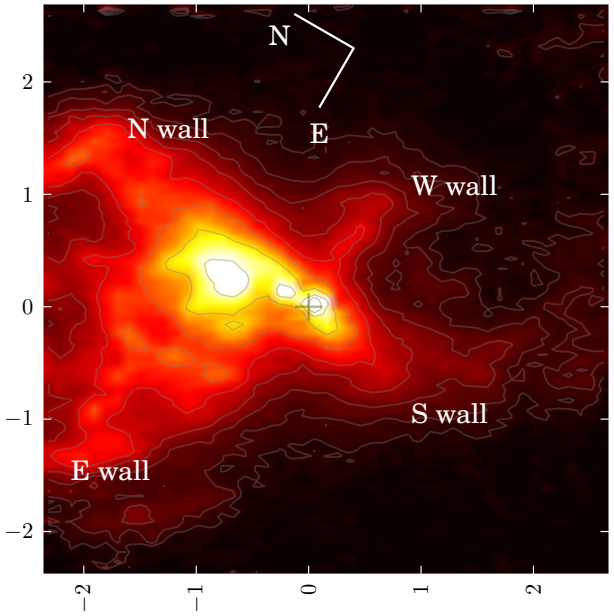


**Figure 2.** Integrated flux map in the [Fe II] $\lambda\,1.644\,\mu$m emission line. Note the hourglass (rather than a conical) shape of this emission. The north, south, east and west walls are indicated by the labels. Spatial units are in arcsec and the position of the nucleus $(0, 0)$ is indicated by a plus sign. The orientation is indicated by the arrows. Contours are used to best delineate the structures.

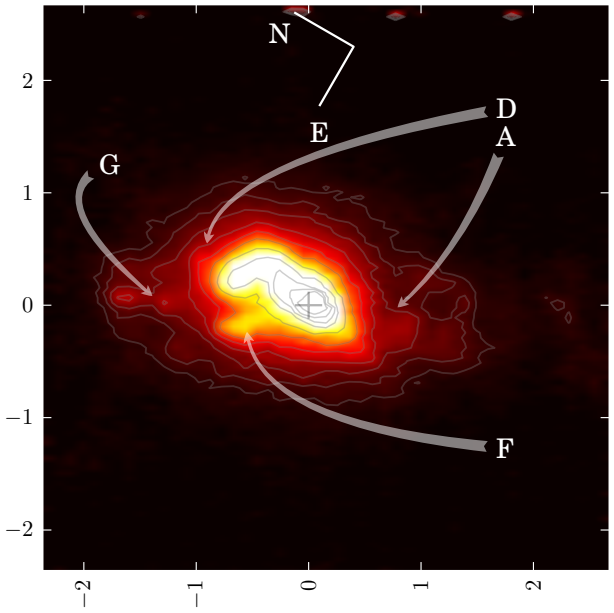


**Figure 3.** Integrated flux map in the Br$\gamma$ line. Details are the same as in Fig. 2, otherwise indicated bellow. The letters A, D, F and G label structures corresponding to those previously identified in the [O III] flux map from Evans et al. (1991).

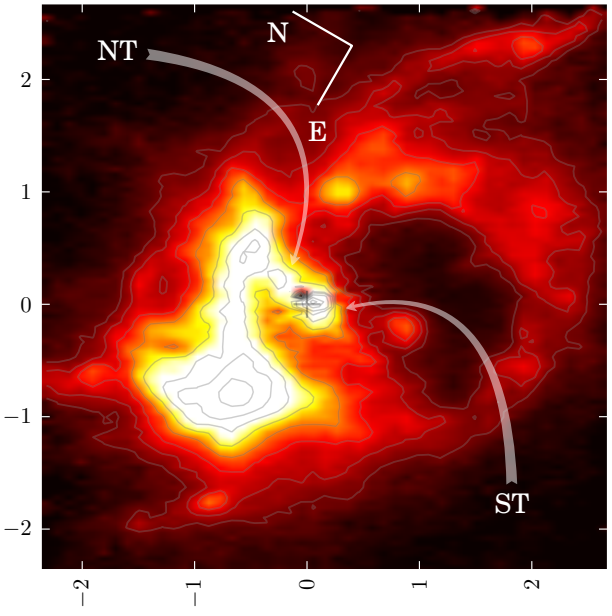


**Figure 4.** Integrated flux map in the $H_2$ 2.12 $\mu$m line. Details are the same as in Fig. 2, otherwise indicated bellow. NT and ST identify the northern and southern "tongues" from Müller Sánchez et al. (2009).

using velocity channel maps and position-velocity (hereafter *p-v*) diagrams. These two types of maps are two-dimensional cuts through the 3D integral field data: the channel maps are cuts across the wavelength (velocity) axis and the *p-v* diagrams are cuts across one of the position axes.

The channel maps are presented in Figures 5 to 8 and show emission line flux distributions in velocity channels along the line profile from blueshifts to redshifts after the subtraction of the systemic velocity of the galaxy, adopted as 1137 km s$^{-1}$ (Huchra, Vogeley & Geller 1999). Each velocity channel integrates 3 pixels in the velocity axis corresponding to 87.6 km s$^{-1}$ for [Fe II] and 88.7 km s$^{-1}$ for Br$\gamma$ and 2 pixels in $H_2$ corresponding to 60.3 km s$^{-1}$. The central velocity $v$ is written at the bottom of each panel. The central velocities were chosen so that the velocity range covers all the line profile from blueshifts to redshifts. In all panels we draw an auxiliary dashed gray line indicating the orientation of the galactic line of nodes adopted as 80°, as obtained from the observation of the stellar kinematics of the inner regions by Storchi-Bergmann et al. (2012). The N and E arrows show the orientation of our images in the sky and the label "far side" indicates the far side of the galactic disc.

The *p-v* diagrams are presented in Figures 6 and 9 for [Fe II] and $H_2$, respectively. The bottom right panel depicts the integrated flux map of the line showing the slits of the *p-v* diagrams running horizontally in the figure. In the *p-v* panels the velocity runs along the horizontal axis (PA = 30°) and the position along the vertical axis with NE at the bottom (negative positions) and SW at the top (positive positions). In the top left of each *p-v* panel the central position of the slits is written in arcsecs.

In the next subsections we describe the channel maps and *p-v* diagrams for the ionized and molecular gas as well as our interpretation.

### 4.1 [Fe II]

#### *4.1.1 Channel Maps*

The [Fe II] channel maps are shown in Fig. 5, where we see emission in velocity channels from $-723$ km s$^{-1}$ to 590 km s$^{-1}$. In fact we found [Fe II] emission in velocity channels ranging from about $-1500$ km s$^{-1}$ to 770 km s$^{-1}$. The channels not shown in the figure were omitted because they present a structure that does not change much from what is seen in the first and last channels. The emission seems to extend beyond the instrument field of view in the majority of the panels. The central and redshifted panels delineate a "bowl" shape which can also be described as similar to an hourglass extending along the horizontal direction in our images, from NE to SW with axis along PA $\sim 30°$. This hourglass seems to correspond to the walls of the bipolar outflow modelled by (Das et al. 2006) with a hollow cone shape. The walls of this structure are oriented approximately along N and E to one side of the nucleus and along S and W to the other side.

The highest blueshift structures detached from the nucleus are observed in the NE outflow up to a velocity channel centered at $-1249$ km s$^{-1}$ (not presented in the figure).

The N wall of the hourglass is observed covering a range of blueshifts and redshifts, while the E wall is observed mostly in redshift. The N and E walls of the hourglass do not keep the same PA and structure over the velocity channels due to the patchy nature of the emitting gas and also because of the hourglass geometry and its relative orientation to the line of sight. The opening angle of the walls is widest ($\sim 100°$) at the low redshift channels.

The S wall is observed mostly in blueshift, while the W wall is the faintest, observed in the lowest velocity channels.

The most luminous part of the outflow is the "fan-like" structure observed to the NE in the redshift channels, corresponding to the back wall of the NE outflow.

Radio MERLIN 18 cm, VLA 6 cm and MERLIN 6 cm contours are superimposed, respectively, to the panels with velocities 327 km s$^{-1}$, 415 km s$^{-1}$ and 503 km s$^{-1}$. The MERLIN 18 cm emission fills the region between the N and E walls of the hourglass and also extends towards SW partially filling that side of the hourglass. The MERLIN 6 cm is very compact and extends towards NE at PA $\sim 30°$ along the axis of the hourglass. The VLA 6 cm radio image is more extended than the MERLIN 6 cm. Its emission partially fills the NE side of the hourglass and has a detached patch of emission to the SW.

In the velocity channel map at 65 km s$^{-1}$, the contours of the *HST* [O III] integrated flux image are shown. The emission covers most of the field and extends toward NE along PA $\sim 30°$. There is good correspondence between [O III] and [Fe II] flux distributions within 1 arcsec from the nucleus between N and NE at the highest flux levels. At lower flux levels the correspondence is poorer and in the [O III] contours we do not see the "bowl"shape seen in the [Fe II] flux distributions of the redshift channels.

#### *4.1.2 Position Velocity Diagrams*

Fig. 6 presents the [Fe II] *p-v* diagrams in panels corresponding to adjacent slits 0.″13 wide. The lower right panel of the figure presents the integrated [Fe II] emission line flux map. Despite our efforts to clean all artifacts from the data, regularly spaced vertical lines resulting from the continuum subtraction appear in velocities $-750$ km s$^{-1}$, $-250$ km s$^{-1}$, 250 km s$^{-1}$ and 750 km s$^{-1}$ mainly in the central panels and should not be confused with real structures by the reader.

The *p-v* flux distribution is dominated by emission from the NE side of the outflow in most panels (lower half of the panels) although weak emission from the galactic disc is also seen running vertically at $v = 0$ km s$^{-1}$. The most prominent feature is an inverted "v"-shaped structure which appears in slits ranging from 1.″08 to 0.″00 therefore coming mainly from the N side of the hourglass structure. This structure is indicated in the panel corresponding to the slit 0.″27 by solid straight lines and the label "Inv. V". We observe that this feature is asymmetric with the blueshift side reaching almost twice as much velocity as the redshift side for equivalent distance from the nucleus.

We have also identified in Fig. 6 the emission coming from the W wall – observed in the slits 0.″94 to 0.″13 (label "W wall"), and that coming from the S wall – observed in the slit positions 0.″00 to -0.″81 (label "S wall").

In the slits corresponding to negative positions up to 0.″00 we see the kinematic signatures of many individual high velocity dispersion clouds (labeled HVDC) identifiable as horizontally elongated emitting areas. The velocity dispersion of these structures range from $\sim$ 300 km s$^{-1}$ to $\sim$ 900 km s$^{-1}$. Each cloud appears in two or three adjacent panels indicating they have angular sizes ranging from 0.″2 to 0.″4. These clouds originate in the front wall of the NE side of the hourglass.

### 4.2 Br$\gamma$: Channel Maps

The Br$\gamma$ channel maps are shown in Fig. 7, where we see emission in velocity channels ranging from $-1022$ km s$^{-1}$ to 663 km s$^{-1}$. We, however, found Br$\gamma$ emission in velocity channels ranging from about $-1110$ km s$^{-1}$ to redshifts beyond 1000 km s$^{-1}$. The omitted channels beyond redshift 663 km s$^{-1}$ show only the central component getting fainter with redshift and the channel $-1110$ km s$^{-1}$ shows a faint similar structure to that seen in the channel $-1022$ km s$^{-1}$.

The emission structure is more compact than that seen in the [Fe II] channels and is composed mainly by emission to the N-NE seen in both blueshifted and redshifted channels and to the SW in channels from $-331$ km s$^{-1}$ to 663 km s$^{-1}$.

The contours of the *HST* [O III] line emission are overplotted on four channels corresponding to the velocities $-756$ km s$^{-1}$, $-135$ km s$^{-1}$, 308 km s$^{-1}$ and 485 km s$^{-1}$. These are the same contours as those overplotted in the [Fe II] channel maps. The correlation between the [O III] contours and Br$\gamma$ flux distribution is better than that between [O III] and [Fe II]. Almost every Br$\gamma$ feature (covering the whole velocity range) corresponds to an [O III] feature. In particular we identify (from Evans et al. 1991) in Fig. 7 the components A, C, D, F and G which are observed in blueshift, component E observed in blueshift and redshift and component B, the nuclear component, observed in all velocity channels.

We have also identified some new structures in the SW side of the bipolar outflow which we call B1, R1 and R2. B1 is observed in the velocity channels from $-224$ km s$^{-1}$ to

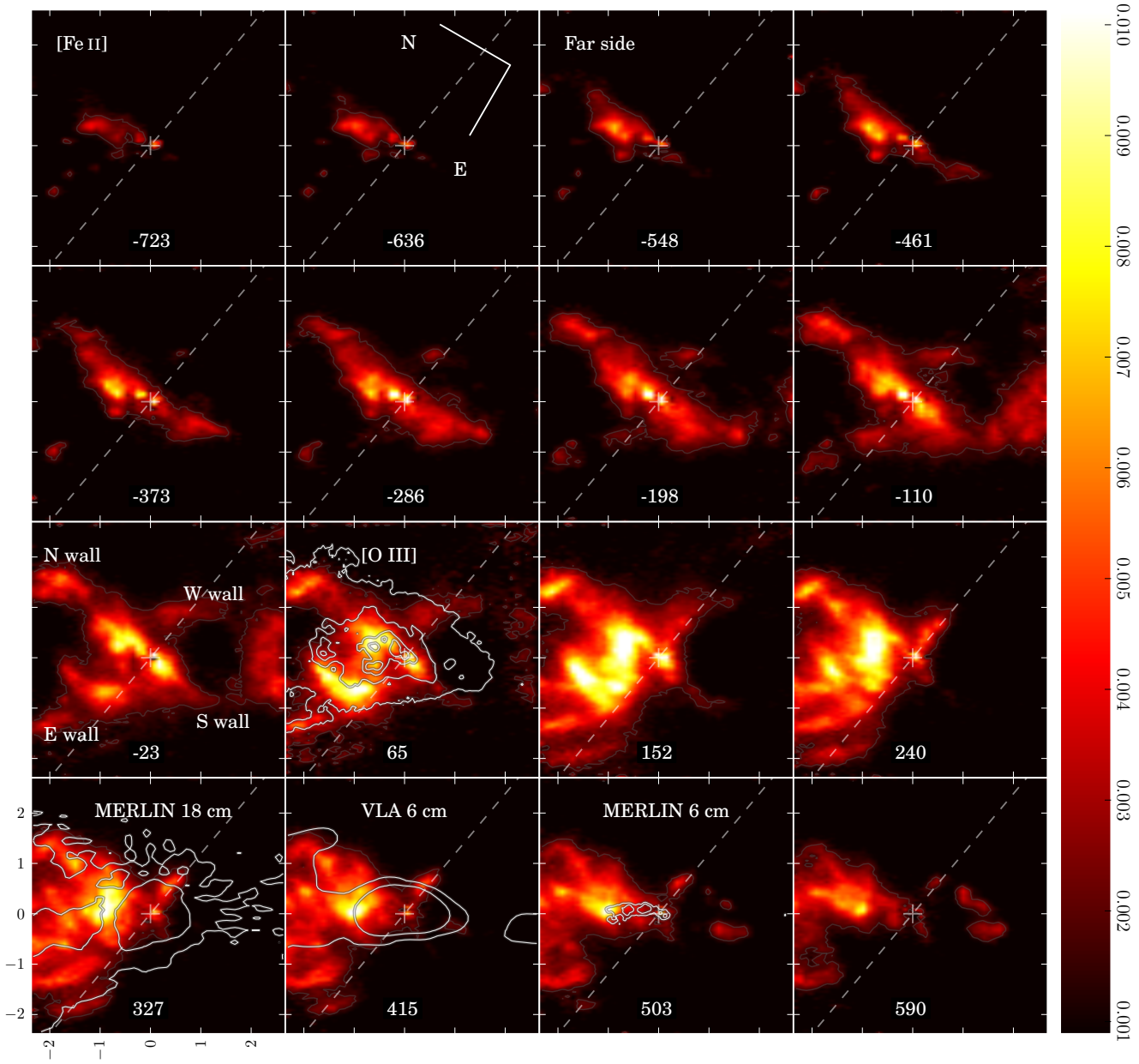


**Figure 5.** Channel maps of the [Fe II] line. The channel velocities are written in the central bottom side of every panel and are given in km s$^{-1}$. The line of nodes is indicated by the dashed gray line and the assumed far side of the galaxy is indicated in the panel with velocity $-548$ km s$^{-1}$. The orientation is indicated by the arrows in the panel with velocity $-636$ km s$^{-1}$. The N, E, S and W walls are indicated in panel with velocity $-23$ km s$^{-1}$ The radio contours of MERLIN 18 cm, VLA 6 cm and MERLIN 6 cm are overlaid, respectively, in the panels with velocities 327, 415 and 503 km s$^{-1}$ and [O III] contours are shown in the panel with velocity 65 km s$^{-1}$. A color bar on the right gives the correspondence between color tones and flux in units of $10^{-15}$ erg cm$^{-2}$ s$^{-1}$ Å$^{-1}$.

$-47$ km s$^{-1}$ as an area of faint Br$\gamma$ emission indicated in panel of $v = -135$ km s$^{-1}$. This area has a SE-NW extension of about $2''$ and is observed at $\sim 2$ arcsec SW of the nucleus, although it seems to extend to SW beyond the field of view. We attribute this emission to the front wall of the SW outflow. R1 and R2 are two redshift components (shown in panels of $v = 397$ km s$^{-1}$ and 663 km s$^{-1}$ respectively). R1 is observed in the velocity range 131 km s$^{-1}$ to 574 km s$^{-1}$ at $\sim 1\farcs2$ SW of the nucleus at PA $= 193°$ and R2 in the velocity range 397 km s$^{-1}$ to 751 km s$^{-1}$ distant from the nucleus by $\sim 1\farcs2$ at PA $\sim 210°$. We atribute the origin of R1 and R2 to the back wall of the SW outflow. Direct comparison of the [O III] contours to the Br$\gamma$ flux map at the positions of R1 and R2 reveals a correspondence of [O III] emission to the Br$\gamma$ components. These redshift components are also observed in [Fe II] in channels from 327 km s$^{-1}$ to 678 km s$^{-1}$ for R1 and in channels from 503 km s$^{-1}$ to 678 km s$^{-1}$ for R2. R1 and R2 are, respectively, in vertical coordinates $-0.3$ and 0.1 arcsec approximately and, therefore, are separated by $\simeq 0.4$ arcsec.

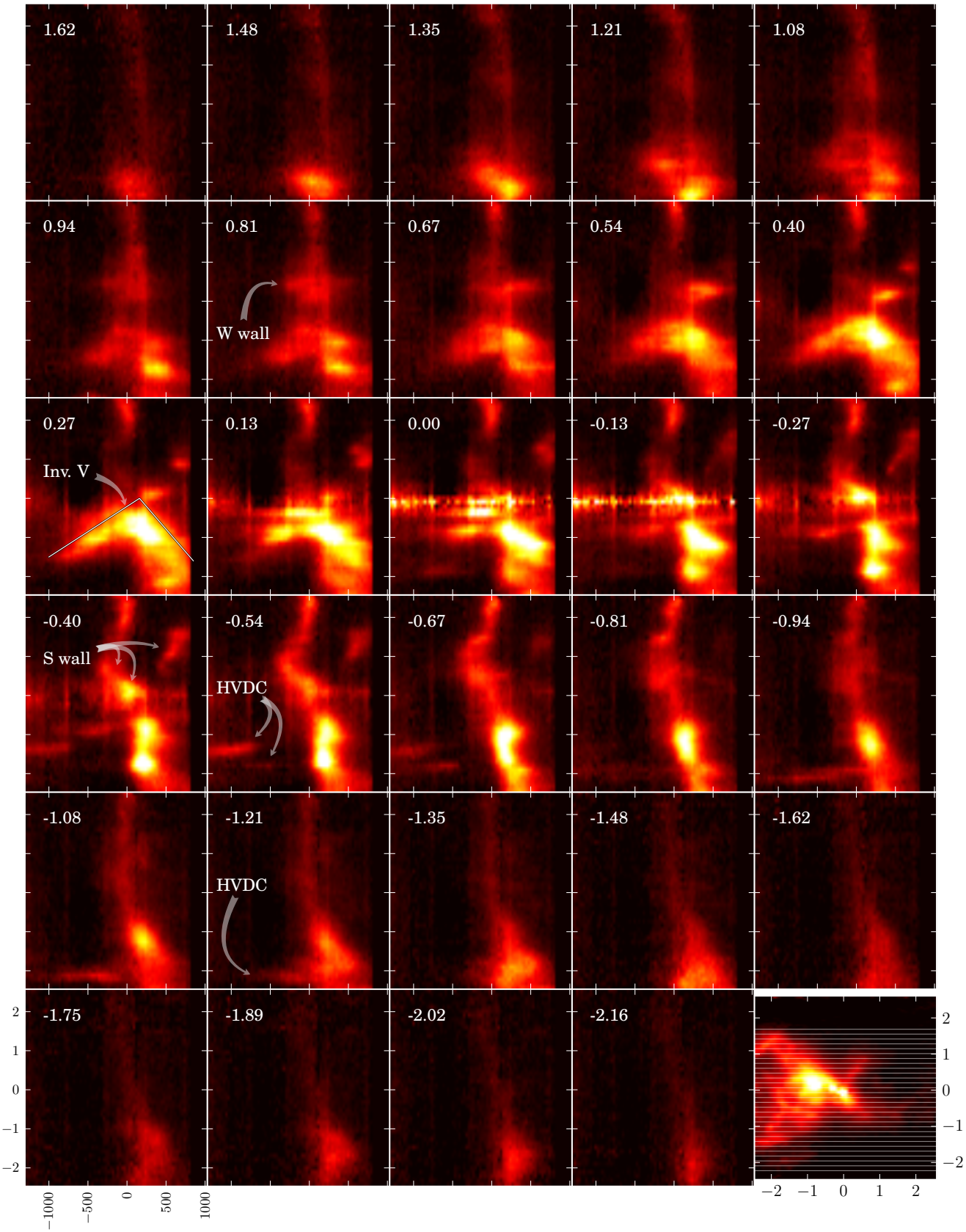


**Figure 6.** *p-v* diagram of the [Fe II] line. The numbers in the panels correspond to the slit centre position relative to the nucleus along the 'y' axis of our data. The slits are indicated by the horizontal solid lines overlaid in the [Fe II] integrated flux map shown in the lower right panel. Vertical stripes seen at velocities −750 km s$^{-1}$, −250 km s$^{-1}$, 250 km s$^{-1}$ and 750 km s$^{-1}$ are artifacts.

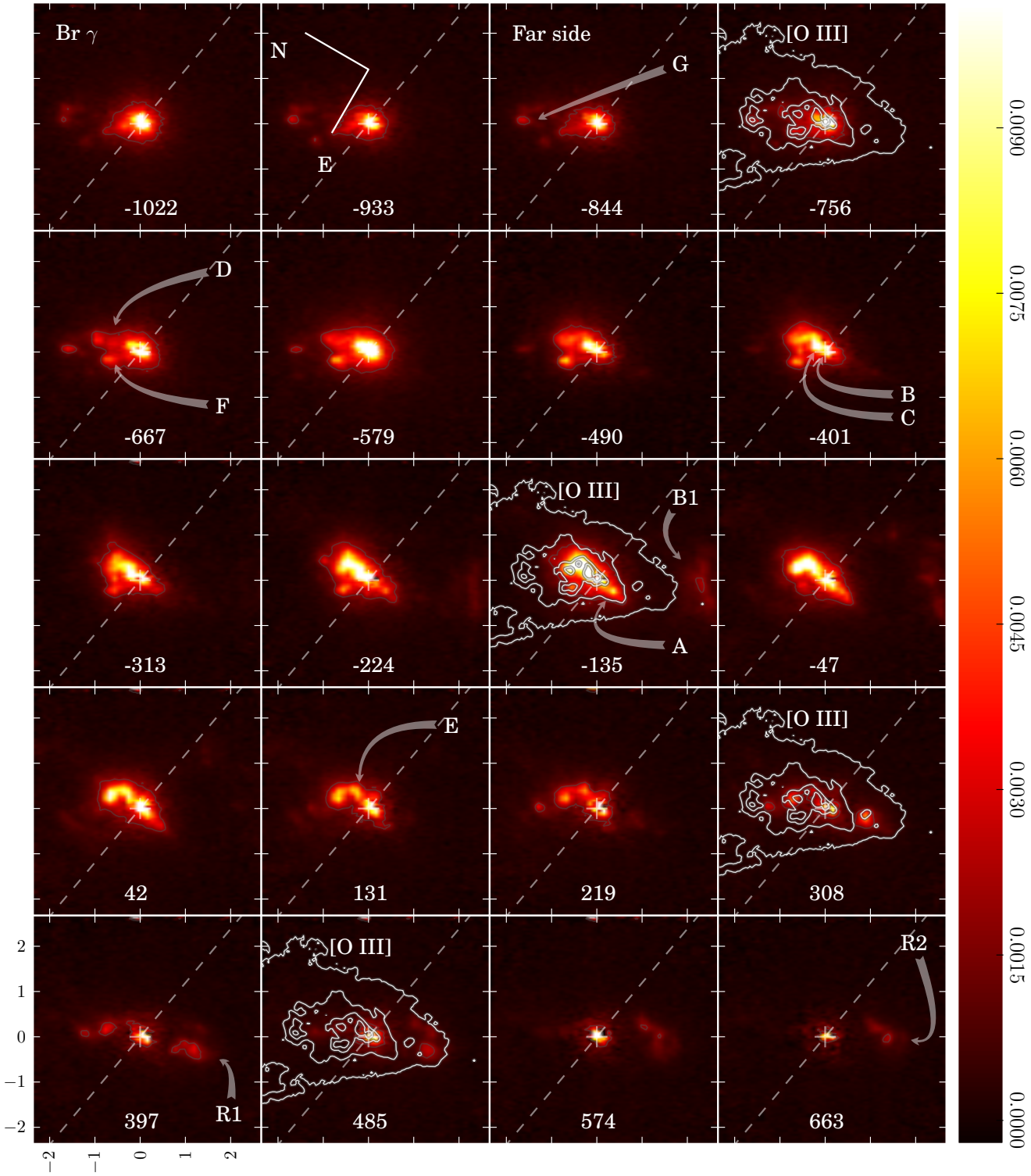


**Figure 7.** Channel maps of the Br$\gamma$ line. The velocities are written in the central bottom part of every panel and are given in km s$^{-1}$. The major axis is indicated by the dashed gray line and the assumed far side of the galaxy is indicated in the panel with velocity $-844$ km s$^{-1}$. The orientation is indicated by the arrows in the panel with velocity $-933$ km s$^{-1}$. The [O III] contours are overlaid in the panels with velocities $-756$, $-135$, 308 and 485 km s$^{-1}$. A color bar on the right gives the correspondence between color tones and flux in units of $10^{-15}$ erg cm$^{-2}$ s$^{-1}$ Å$^{-1}$.

### 4.3 Interpretation: Ionized gas kinematics

The ionized gas kinematics has been previously modeled by Das et al. (2006) as a bi-conical outflow with axis at PA = 30° in which the front walls produce the blueshifted emission and back walls, the redshifted emission. Their model was fitted to [O III] kinematic data measured using HST STIS long-slit spectroscopy. Fig. 7 shows that the flux distribution in [O III] (contours) is very similar to that of Br$\gamma$ and so we assume that their emission originate in the same gas and consequently the kinematics of the [O III] and Br$\gamma$ should also be similar. The blueshift channels correspond to the front wall of the outflow and the redshift channels correspond to the back wall. From this figure it is not clear that the geometry of the outflow is conical as derived by Das et al. (2006). In our data the brightest emission comes, from a narrow region extending from the nucleus to the N-NE, being stronger in the blueshift channels. This emission comes from the front wall of the outflow which is at higher galactic latitude than the emission from the back wall, that is observed in redshift. Additionally, the emission coming from the SW side of the outflow is observed in redshift corresponding to emission from the back wall of the outflow which is at higher galactic latitude than that of the front wall.

Das et al. (2006) derived the conical geometry for the outflow from the kinematics that they could obtain from deep STIS long-slit spectroscopy of the whole region, not from the flux maps.

The approximately conical geometry is better seen in the [Fe II] channel maps (Fig. 5), and in particular, in the redshift channels. While the Br$\gamma$ emission distribution is concentrated and mostly directed towards north, the [Fe II] emission distribution encompasses it and extends further spanning a wide hourglass shaped area more clearly seen to NE of the nucleus between PA = 0° and 90° in the redshift channels.

The difference between [Fe II] and Br$\gamma$ flux distribution and kinematics can be understood as follows. As discussed by Mouri, Kawara and Taniguchi (2000), most of the [Fe II] emission comes from a region where H is only partially ionized. In the completely ionized region, as the ionization potential of Fe+ is just 16.2 eV, Fe+ is further ionized and there is not much [Fe II] emission. Extensive partially ionized zones around the NLR of Seyfert galaxies are created by X-rays that have small cross sections and penetrate deeper in the gas than less energetic photons, heating the gas. The [Fe II] $\lambda\,1.644\,\mu$m emission is excited in these partially ionized zones by collisions with electrons, as well as by shocks that may be present due to the interaction of AGN jets and winds with the ambient gas. The extent of the partially ionized region determines where we may find [Fe II] emission. The larger extent of the [Fe II] emitting region compared to that of the Br$\gamma$ can thus be understood as caused by the existence of a partially ionized zone extending beyond the fully ionized hydrogen zone where Br$\gamma$ is produced.

The enhancement of the [Fe II] emission to the NE in the redshift channels when compared with the Br$\gamma$ emission can also be attributed to the interaction of the back wall of the outflow with the far side of the galaxy disc. The shocks produced in this interaction could provide the energy for the excitation of [Fe II], besides some contribution from collisions with electrons in the gas heated by X-rays from the AGN. Support for the presence of shocks is provided by line ratio maps presented in Paper I. Towards the borders of the line flux distributions, in particular to the NE border, there is an increase of the [Fe II]/Pa$\beta$ line ratio to values up to $\sim 4$, consistent with shock excitation.

We conclude that the [Fe II] emission can be observed beyond the region where [O III] and H recombination lines can be observed, providing a better coverage of the outflow.

### 4.4 $H_2$

#### *4.4.1 Channel Maps*

The $H_2$ emission is detectable mainly in the velocity range $-492$ to 413 km s$^{-1}$ as can be seen in Fig. 8. The distribution of $H_2$ flux emission along the velocity channels is very different from that of the [Fe II] and Br$\gamma$, indicating that they are tracing distinct gas components and processes. The strongest emission is detected in the central channels (around zero velocity) and exhibits a ring like morphology (see Paper I and Müller Sánchez et al. 2009).

The emission of the ring in redshift appears in the velocity channels from 51 km s$^{-1}$ to 232 km s$^{-1}$ and it comes from the N half of the ring while in the blueshift channels from $-250$ km s$^{-1}$ to $-69$ km s$^{-1}$ the emission comes from the S half of the ring.

In the highest blueshift velocity channel we observe nuclear emission as well as a clump of faint emission distant from the nucleus by $\sim 1''$ at PA = 10°. The clump is the tip of an elongated emission structure seen in the channels with velocities $-431$ km s$^{-1}$ to 51 km s$^{-1}$, which include the *northern tongue* (NT as in Müller Sánchez et al. 2009) most clearly seen from channel $v = -69$ km s$^{-1}$ to channel $v = 51$ km s$^{-1}$.

The *southern tongue* (ST as in Müller Sánchez et al. 2009) is identified in channel $v = 51$ km s$^{-1}$ and observable in channels from $v = -69$ km s$^{-1}$ to 51 km s$^{-1}$.

Contours of the *HST* [O III] line emission are overplotted on the velocity channel $-190$ km s$^{-1}$. A comparison of the [O III] contours to the $H_2$ maps shows that the $H_2$ emission knots extending to the N of the nucleus in the blueshift channels also correspond to emission knots in [O III] although the most extended emission is not correlated.

From channel $-190$ km s$^{-1}$ to 293 km s$^{-1}$ we observe the brightest structure, indicated in the channel $-9$ km s$^{-1}$ as BS (for bright spot). This structure appears in our data blended to the ring at NE.

In the highest redshift velocity channel we find faint nuclear emission as well as a clump of emission distant from the nucleus by $\sim 0\farcs9$ at PA = 190°. This redshift clump is identified as HVC (for high velocity cloud) in the velocity channel 353 km s$^{-1}$ and is observed in channels from $v = 293$ km s$^{-1}$ to 413 km s$^{-1}$. This clump is almost symmetrical to the clump seen in the highest blueshift channels suggesting they could be redshift and blueshift counterparts of the same gas ejection event.

#### *4.4.2 Position Velocity Diagrams*

The $H_2$ *p-v* diagrams are shown in Fig. 9. The integrated $H_2$ emission line flux map is shown in the lower right panel.

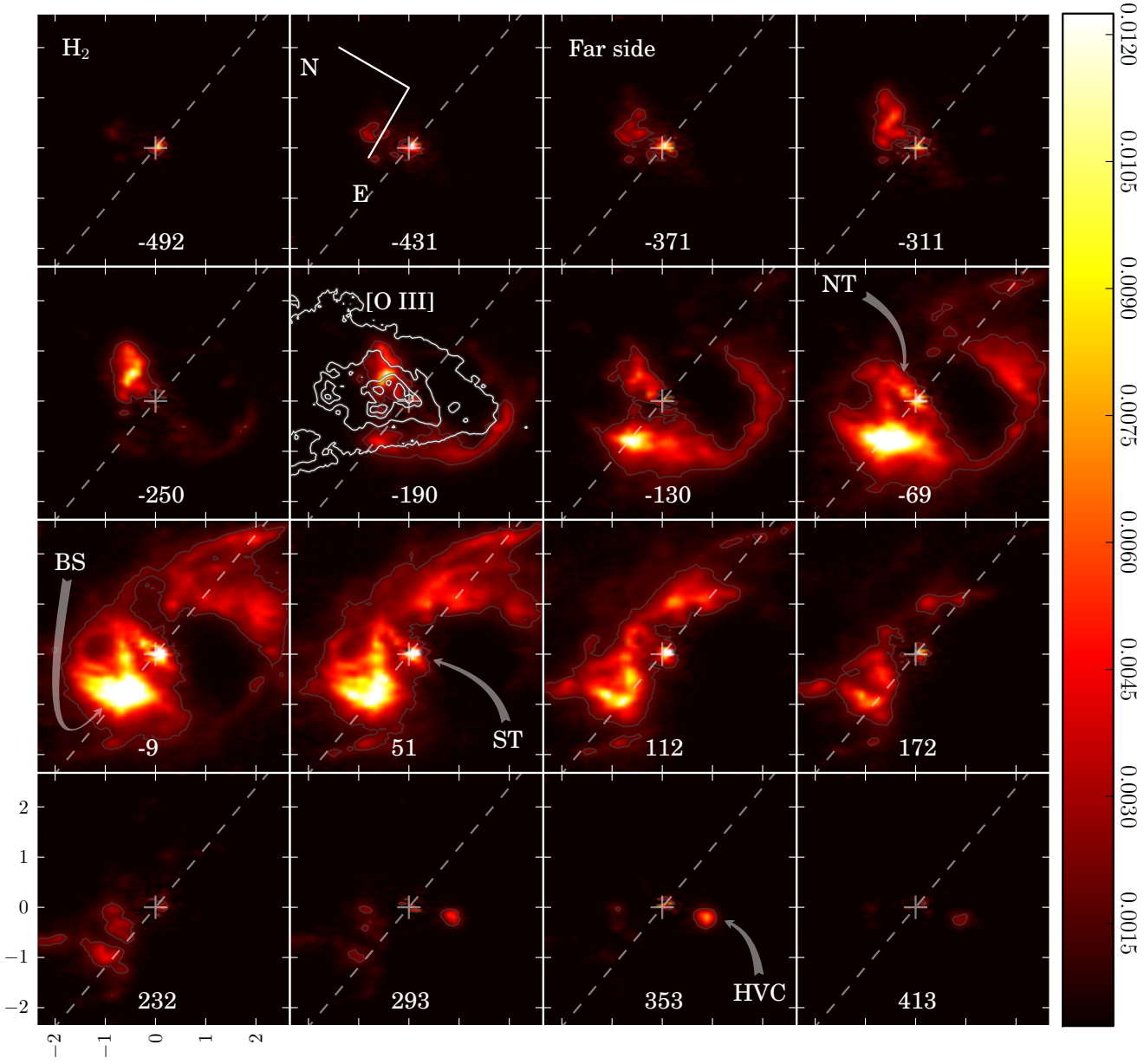


**Figure 8.** Channel maps of the $H_2$ line. The velocities are written in the central bottom part of every panel and are given in km s$^{-1}$. The major axis is indicated by the dashed gray line and the assumed far side of the galaxy is indicated in the panel with velocity $-371$ km s$^{-1}$. The orientation is indicated by the arrows in the panel with velocity $-431$ km s$^{-1}$. The [O III] contours are overlaid in the panels with velocity $-190$ km s$^{-1}$. A color bar on the right gives the correspondence between color tones and flux in units of $10^{-15}$ erg cm$^{-2}$ s$^{-1}$ Å$^{-1}$.

The most conspicuous structures in the integrated flux map are the nucleus, the ring – the NE side being its brightest area, the northern and southern tongues (NT and ST), a bright area to the E of the ring which we call Bright Spot (BS) and an isolated cloud inside the ring, which we call High Velocity Cloud (HVC). It is interesting to note that neither the nucleus nor the HCV are at the centre of the ring.

We describe bellow the structures seen in each *p-v* panel, from the bottom slits (SE) to the top slits (NW). In the panel $-1\farcs76$, there is a high velocity dispersion (hereafter $\sigma$) knot at position $-1''$ with velocities ranging from $\sim -100$ km s$^{-1}$ to $\sim 300$ km s$^{-1}$. The remaining emission in this slit comes from the galactic plane and show velocities around zero, with $\sigma \sim 100 - -200$ km s$^{-1}$. The subsequent slits $-1\farcs58$ and $-1\farcs41$ show similar structures.

From $-1\farcs23$ to $-0\farcs51$ the bright knot of emission at $\approx -0\farcs8$ corresponds to the BS, showing velocities from zero to 300 km s$^{-1}$.

At positive positions, the slits $-1\farcs23$ and $-1\farcs05$ are tangent to the SE side of the ring and its emission has negative velocities reaching up to $\sim -200$ km s$^{-1}$. The emission in this area has a bow figure: around position $0\farcs8$, the velocities are more negative than around position $1\farcs5$ and $0\farcs0$

meaning that as one moves from the inner to the outer border of the ring the velocities change from blueshifts to zero. In the subsequent slits from $-0\farcs87$ to $0\farcs56$, the SW side of the ring shows velocities ranging from $\sim -200$ km s$^{-1}$ at the inner border to zero at the outer border.

In the slits $-0\farcs33$ and $-0\farcs16$ we observe the HVC with a velocity of $\sim 400$ km s$^{-1}$ and $\sigma \approx 100$ km s$^{-1}$.

In the slits from $-0\farcs16$ to $0\farcs74$ the NE side of the ring shows a similar effect to that described above: a velocity gradient across the ring, with the inner part of the ring at position $\sim -0\farcs5$ showing redshifts of up to $\sim 200$ km s$^{-1}$ and the outer part of the ring showing zero velocities.

In the slits $0\farcs02$ to $1\farcs38$ the NT appears at position $\sim -0\farcs6$ with blueshifts of up to $\sim -300$ km s$^{-1}$, and seems to be a structure detached from the ring and from the nucleus.

Finally, the slits $0\farcs74$ to $1\farcs27$ intercept tangentially the NW side of the ring, showing redshifts of 150 km s$^{-1}$ in the inner border of the ring and velocities close to zero in the outer border of the ring.

In summary, a general trend is that the NE side of the ring shows mostly redshifts, while the SW side (which is less luminous) shows blueshifts indicating expansion of the ring. But we, in addition, observe a velocity gradient from velocities in the range 100 – 200 km s$^{-1}$ observed in the inner border of the ring to approximately zero velocities in the outer border of the ring.

### 4.5 Interpretation: Molecular gas kinematics

The $H_2$ kinematics is completely distinct from that of the ionized gas and implies an origin for the $H_2$ in an expanding ring in the galaxy plane while the ionized gas is observed in outflow and extends to high latitudes. This decoupling between molecular and ionized gas is a result commonly found in previous studies of the NLR of active galaxies by our group AGNIFS (Barbosa et al. 2009; Storchi-Bergmann et al. 2009, 2010; Riffel & Storchi-Bergmann 2011a,b; Riffel, Storchi-Bergmann & Winge 2013a).

Although the morphology of the $H_2$ ring suggests it is a circular ring in the plane of the galaxy (Paper I), its kinematics does not suggest rotation. In the redshift channels from 51 km s$^{-1}$ to 232 km s$^{-1}$ the emission comes mostly from the N half of the ring which is in the far side of the galaxy while in the blueshifted channels from $-250$ km s$^{-1}$ to $-69$ km s$^{-1}$ the emission comes from the S half of the ring which is in the near side of the galaxy. Assuming that the ring is in the galactic plane, this kinematics is that of a ring expanding radially at an average velocity of $\approx 100$ km s$^{-1}$. This conclusion can also be reached via the analysis of the *p-v* diagrams (Sec. 4.4.2), in which the NE side of the ring shows mostly redshifts, while the SW side shows blueshifts. For an orientation of the kinematic line of nodes of 80°, these results indicate expansion of ring in the plane. The ring has been also observed in CO millimeter emission lines by Krips et al. (2011) who also concluded that it is expanding.

But in the *p-v* diagrams we have observed something else: a velocity gradient across the ring, in which velocities of up to 200 km s$^{-1}$ are observed in the inner border of the ring (which are positive in the far side and negative in the near side) and velocities close to zero in the outer border of the ring. This result indicates that the expansion in the ring has negative acceleration. This deceleration, showing that the outer border of the ring is not expanding anymore allows to reconcile our previous finding in Storchi-Bergmann et al. (2012), that the $H_2$ ring is also the site of a young (age $\approx 10$ Myr) stellar population, with the ring kinematics. If the ring were expanding at constant velocity of $\sim 100$ km s$^{-1}$, as previously thought, the 100 pc ring would have moved away by much more than 100 pc in $10^7$ yr, and there should be no association anymore between the $H_2$ ring and star formation originated in this same gas.

Hydrodynamic jet simulations by Gaibler et al. (2012) support the formation of rings of young stellar population in the galaxy disc as a result of shock waves created during the early phases of the jet activity when the jet is still contained inside the galactic disc. They predict that these rings should have a radius of $\sim 100$ pc. The ring is formed by the expansion of gas pushed by the shock waves produced by the jet which eventually stop and pile up leading to the formation of the young stars. The $H_2$ ring we detected in correspondence to the ring of young stellar population (Storchi-Bergmann et al. 2012) has the right size and kinematics predicted by the model of Gaibler et al. (2012). Only that the ring is not centered at the nucleus, as predicted by the model. One possibility to explain this is the presence of inhomogeneities in the gas density and distribution around the nucleus that could lead to the off-centered appearance after the expansion.

Müller Sánchez et al. (2009) modeled the $H_2$ kinematics in the inner tens of pc's and proposed that there are two streams of molecular gas towards the nucleus (indicated by NT and ST in Fig. 8). In their model the ST is in front of the central source obscuring it and flowing into it. In their measurements the NT has an almost constant velocity of $-25$ km s$^{-1}$ and the ST shows an increase in velocity from 30 km s$^{-1}$ at $r = 0\farcs4$ (distance from the nucleus) to 90 km s$^{-1}$ at $r = 0\farcs04$. In our data the ST has redshift velocities spanning the range 0 to 200 km s$^{-1}$ as can be seen in Fig. 9 in slits 0.02 and $-0.16$ arcsec. The NT has blueshift velocities in the range 0 to $-300$ km s$^{-1}$ as seen in the slits 0.2, 0.38 and 0.56 arcsec. These velocities seem incompatible with those of Müller Sánchez et al. (2009).

The analysis of our data led us to propose an alternative scenario for the dynamics of the $H_2$ NT and ST structures. The NT gas emission is projected in the plane of the sky co-spatially to the brightest Br$\gamma$ emitting structure which is seen in the channels $-47$ km s$^{-1}$ to $-313$ km s$^{-1}$ and is interpreted as gas in outflow at high galactic latitude. In order to survive, the molecular gas in the NT must be shielded from the ionizing radiation. We propose that the ionized gas pushes molecular gas which is thus also observed in outflow. The same scenario is also proposed for the ST with the difference that this component surrounds the ionized gas in redshift which consequently produces $H_2$ velocities in the redshift domain. Additionally we note that in our data (as well as in those from Müller Sánchez et al. (2009)) the NT is brighter than the ST suggesting that the NT is in front of the galactic disc and the ST is behind the galactic disc.

In above scenario the $H_2$ emission is not restricted to the galaxy plane. We show in Figure 10 a comparison between the $H_2$ (green) and [Fe II] (red) kinematics via their channel maps. In the channels $-360$ km s$^{-1}$ and $-200$ km s$^{-1}$ there is a $H_2$ structure to the N which does not seem to be in the galaxy plane. This structure seems to connect to the

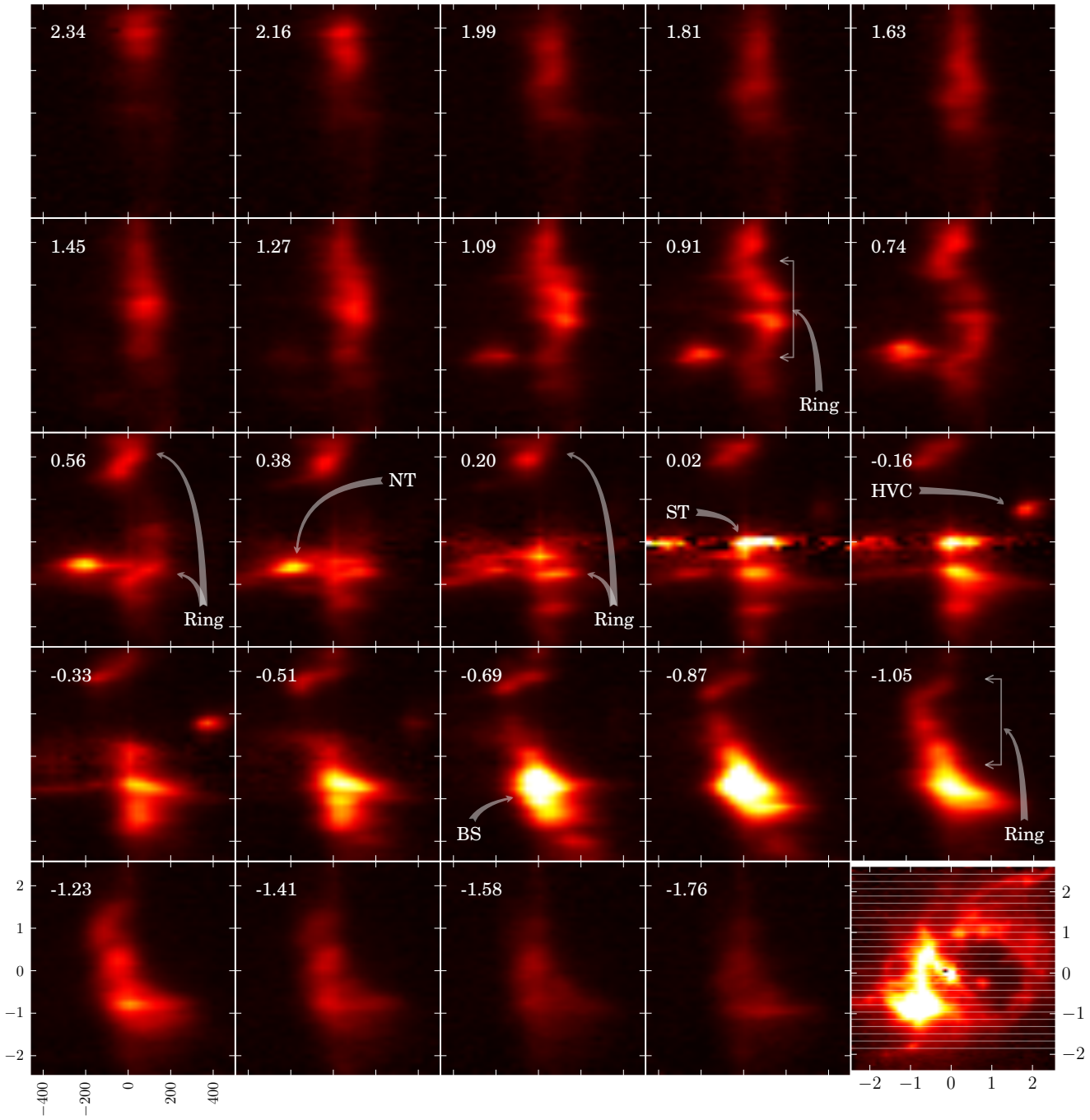


**Figure 9.** *p-v* diagram of the $H_2$ line. The numbers in the panels correspond to the slit position relative to the nucleus along the 'y' axis of our data. The slits are indicated by the horizontal solid lines overlaid in the $H_2$ integrated flux map shown in the lower right panel.

NT at the channels $-120$ km s$^{-1}$ and $-40$ km s$^{-1}$ supporting that the NT originates in gas that is not in the plane. In fact in the channel $-40$ km s$^{-1}$ the yellow color indicate that the NT is superimposed to the N wall of the [Fe II] outflow. Other superposition regions (yellow color) between $H_2$ and [Fe II] appear in the BS area in channels 40 km s$^{-1}$ and 120 km s$^{-1}$ which suggest that the enhanced $H_2$ emission there is related to the outflow observed in [Fe II]. Another high velocity structure which does not seem to be in the plane is the HVC seen from channels 280 km s$^{-1}$ and 440 km s$^{-1}$. This structure seems to be associated to the R1 which we interpret as part of the back wall of the SW side of the outflow (see 4.3).

## 5 OUTFLOW MODELS

The [Fe II] integrated flux map presents an emitting structure with the shape similar to an hourglass with axis along

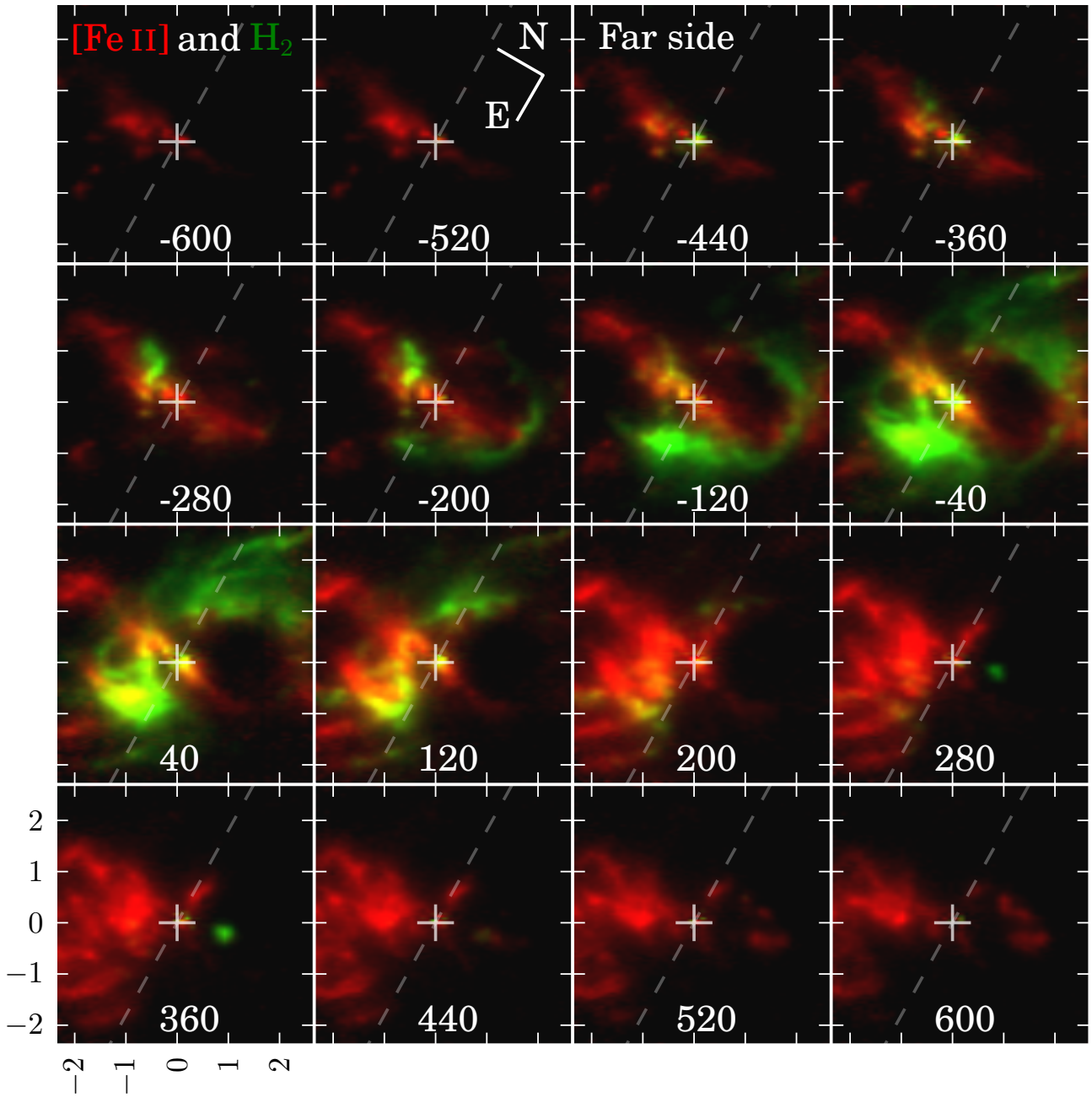


**Figure 10.** Comparison between the [Fe II] (red) and $H_2$ (green) kinematics. The dashed line shows the line of nodes. The center cross marks the position of the nucleus. The other labels are as in previous figures.

the direction NE to SW. The NE side is brighter and more extended than the SW side.

Das et al. (2006), using *HST/STIS* long slit spectroscopic [O III] data proposed a kinematic model in which a hollow conical outflow first accelerates from zero to 2000 km $s^{-1}$ then decelerates to zero. The radial distance from the nucleus where the velocity reaches its maximum value is 140 pc and where the velocity returns to zero is 400 pc. The inner and outer cone aperture angles are, respectively, 20° and 40°. The PA and the inclination of the cone axis relative to the plane of the sky are 30° and 5°, respectively. We have implemented this model and compared its predictions to our [Fe II] kinematics. The deviations from the model predictions to the [Fe II] kinematics led us to try distinct models but having it as a starting point.

### 5.1 Conical outflow model

In Figure 11 we present the [Fe II] integrated flux map compared to the flux map obtained for a hollow conical outflow model similar to that of Das et al. (2006). The model shows rough correspondence to the data but the opening angle of

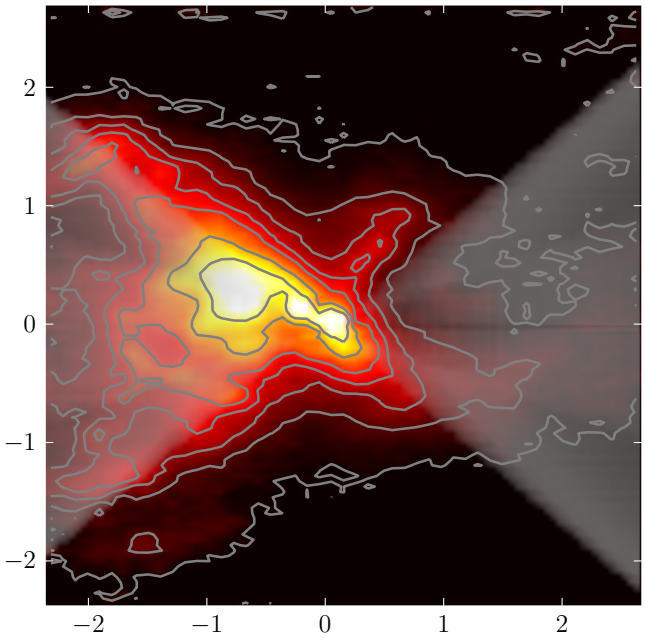


**Figure 11.** [Fe II] integrated flux map (hot colours) and hollow conical outflow model (grey levels).

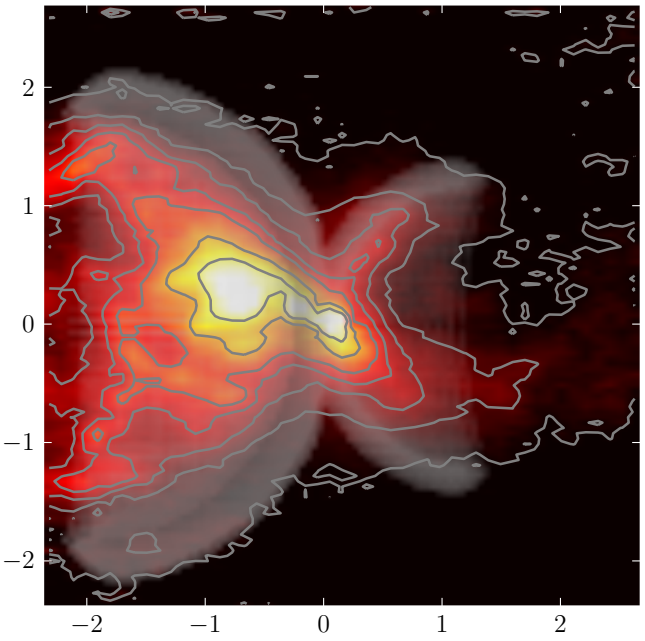


**Figure 12.** [Fe II] integrated flux map (hot colours) and hollow spherical outflow model (grey levels).

the cone is smaller than the opening angle we see in the data. We also note that the flux map shows a change of the opening angle with distance from the nucleus.

The conical model shown here is a modified version of the Das et al. (2006) model in which the maximum velocity is lower, namely 1000 km s$^{-1}$ instead of 2000 km s$^{-1}$ as it provided a better fit to our data. In our data we do not see a decrease in velocity within our field-of-view therefore we further modified the model to keep the velocity at the maximum value up to the borders of the field. Besides these changes in velocity domain, the other parameters of their cone model were kept the same.

Summarizing, the model consists of an accelerated hollow conical outflow with internal and external half-opening angles $\theta_{\rm inner} = 20^\circ$ and $\theta_{\rm outer} = 40^\circ$ respectively, inclination and position angle of the bicone axis, respectively, $i_{\rm axis} = 5^\circ$ (northeast is closer) and $\mathrm{PA}_{\rm axis} = 30^\circ$, the radius where the maximum velocity occurs $r_t = 80$ pc and the maximum velocity $v_{\rm max} = 1000$ km s$^{-1}$.

The comparison between the [Fe II] and the model is shown in Fig. 1 of the Appendix (available online as a supplementary material).

Comparison of the model with the data shows good correspondence in low velocity redshift channels to the NE. The highest blueshift channels seem to show poor agreement but this may be due to the fact that the actual outflow is patchy, in particular in the regions corresponding to the front wall of the NE side of the outflow. To the SW, most of the outflow is either also very patchy or hidden behind the galactic disc.

The $p$-$v$ diagrams of the hollow conical outflow model are compared to the [Fe II] data in Fig. 2 of the Appendix (available online as a supplementary material). The model shows good agreement with the data mainly in the redshift side of the NE emission (bottom right of the diagrams). The $p$-$v$ structures to the SW side show poor agreement but, as pointed out above, this is due to the patchy nature of the outflow and because the SW side is partially hidden by the galactic disc.

### 5.2 Spherical outflow model

In order to address the morphological differences between the data and the conical model and to try to meet the broader shape of the outflow at its base we next implemented a hollow spherical outflow model with constant velocity. The model consists of two thick spherical cavities with centres along the outflow axis separated by a distance $r_1 + r_2$ (where $r_1$ is the radius of the sphere to the NE and $r_2$ is the radius to the SW) so that the spheres touch each other at the nucleus. The outflow is truncated at the distance of one radius from the nucleus to both sides so that only the hemispheres close to the nucleus compose the model. The thickness of the spherical walls was set to $0.2\,r$.

The flux map of the data and model is shown in Figure 12. The spherical model has radii $r_1 = 140$ pc and $r_2 = 93$ pc, maximum velocity $v_{\rm max} = 800$ km s$^{-1}$, inclination and position angle of the symmetry axis $i_{\rm axis} = 5^\circ$ (northeast is closer) and $\mathrm{PA}_{\rm axis} = 30^\circ$, respectively.

The spherical model did not fit well the data for any combination of the parameter values. This can be seen in Fig. 3 of the Appendix (available online as a supplementary material). The $p$-$v$ diagrams of the hollow spherical outflow model are presented in Fig. 4 (only for a few slits) of the Appendix (available online as a supplementary material). We conclude that this model is not a good fit to the data.

### 5.3 Lemniscate outflow model

With the spherical model not being able to reproduce the data we used a shape which is "intermediate" between a conical and a spherical shape, with conical apex (at nucleus) and changing opening angle as a function of distance to the nucleus. We used the shape of a Lemniscate (plot in Figure 13), defined by the expression:

$$(x^2 + y^2)^2 = a^2(x^2 - y^2). \quad (1)$$

The parameter $a$ is the horizontal length of the lemniscate. Solving eq. 1 for $y$ in the domain $x > 0$ we obtain

$$y = \pm\frac{1}{\sqrt{2}}(\sqrt{8x^2a^2 + a^4} - 2x^2 - a^2)^{\frac{1}{2}}. \quad (2)$$

This equation draws the right side of the lemniscate (solid black line in Fig. 13) and it is straightforward to verify that its opening angle at the origin is always 90°. In order to construct a physical model with this shape we must be able to define a wall with finite width. A first approach to accomplish this is to define internal and external limits using lemniscates with different sizes and populating the model in between. The problem in using lemniscates with different sizes is that they always have 90° opening angles at the origin and, therefore, close to the nucleus the wall would have near zero width (see Fig. 13) which, in turn, gives a region with no data. We, then, modified eq. 2 to allow to set the desired opening angle multiplying the whole equation by $\tan(\frac{\alpha}{2})$:

$$y_2 = \tan(\frac{\alpha}{2})\ y, \quad (3)$$

where $\alpha$ is the desired opening angle and $y_2$ is the new function for the lemniscate. The new generated geometry is that of a modified lemniscate which has improved properties relative to the conical and spherical models: an adjustable opening angle at the apex which decreases as a function of distance to the nucleus.

In the velocity domain, this model consists of an acceleration region close to the nucleus, as in the conical model, where the velocity increases from zero at the nucleus to the maximum value $v_{\rm max}$ at $r_t$ followed by a region of constant velocity where the velocity is kept the same up to the limits of the field.

The adopted parameters and their values are: the size of the internal and external lemniscates which are, respectively $a_{\rm inner} = 405$ pc and $a_{\rm outer} = 450$ pc, the internal and external half-opening angles $\theta_{\rm inner} = 35°$ and $\theta_{\rm outer} = 55°$ respectively, the inclination of the lemniscate axis $i_{\rm axis} = 5°$ (northeast is closer), the position angle of the lemniscate axis $\rm PA_{axis} = 30°$, the radius where the maximum velocity occurs $r_t = 80$ pc and the maximum velocity $v_{\rm max} = 1000$ km s$^{-1}$.

The integrated flux map of the lemniscate model is shown in Figure 14 overlaid to the [Fe II] data. Analysing only the morphological and geometrical aspects, the lemniscate model shows some improvement over the conical model.

In Figure 15 we present the channel maps for the data (hot colours) and the hollow lemniscate model (grey levels) superimposed. For most of the channels, there is a better agreement of the model with the data than in the previous two models. The exceptions are the highest redshift channels ($v > 510$ km s$^{-1}$), but, as we already discussed, we have to consider that the outflow is patchy and that most of the SW outflow is hidden behind the galaxy plane. Taking this fact into account, the match between the data and model is very good.

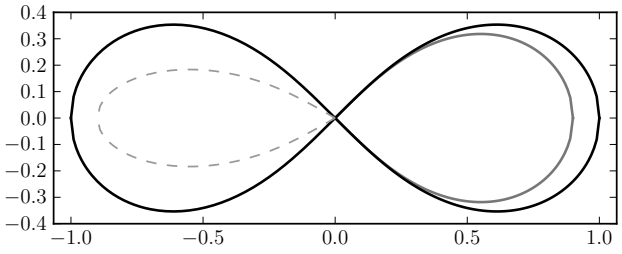


**Figure 13.** The solid black line is a regular lemniscate. The solid gray line (drawn to the right only) is a regular lemniscate with scale parameter $a$ reduced by 10 per cent. The dashed gray line (seen only at left) is a modified lemniscate with opening angle equal to 60° and scale parameter $a$ reduced by 10 per cent.

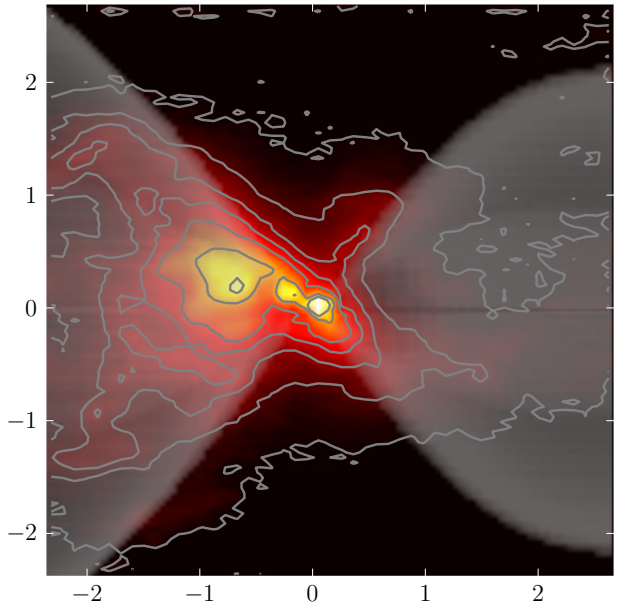


**Figure 14.** [Fe II] integrated flux map (hot colours) and hollow lemniscate outflow model (grey levels).

The $p$-$v$ diagrams of the hollow lemniscate outflow model are compared to the data in Figure 16. There is good agreement to the data, mainly in the redshift side of the NE emission (bottom right of the diagrams) Again, the patchy nature of the outflow and the fact that the SW side of the outflow is behind the galactic disc must be taken into account to explain the discrepancies.

### 5.4 Comparison of the models

Given the distinct morphology of the [Fe II] as compared to that of the [O III] emitting gas and to that of the conical model, it is remarkable that the conical model previously proposed by Das et al. (2006) – based on long-slit spectroscopy – gives such a good reproduction of our [Fe II] data, although we have tuned a bit the parameters. The conical model, however gives a poorer reproduction of the outflow-

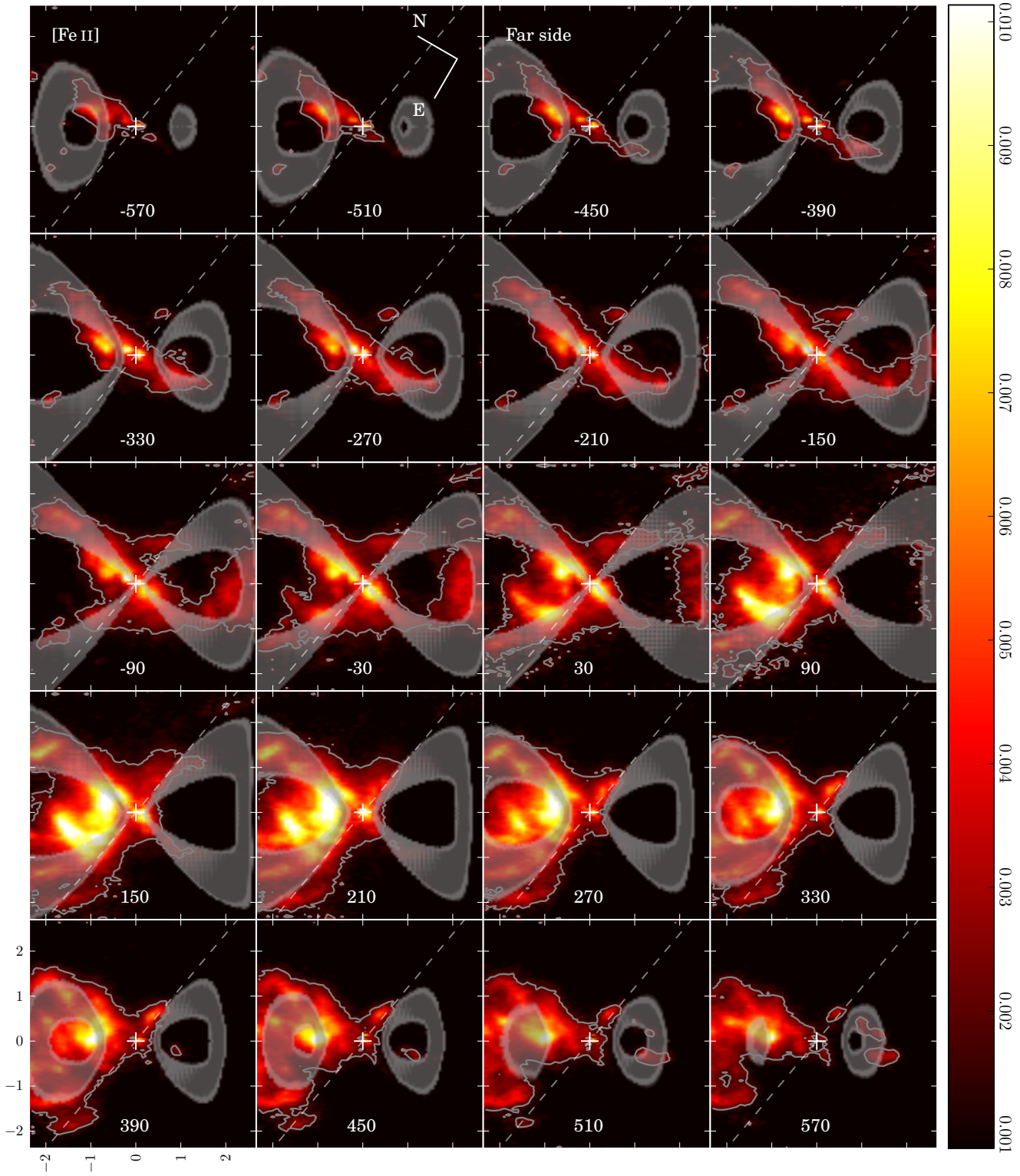


**Figure 15.** Channel maps of the accelerated lemniscate outflow model for the [Fe II] line (grey levels) superimposed to data (hot colours). The data was interpolated in wavelength to the same velocity range as the model. The central velocity of each channel is displayed in km s$^{-1}$ at the bottom of the corresponding panel. The dashed line is the adopted major axis of the galaxy. The tick labels are given in arcsec in the lower left panel. The orientation and adopted far side are indicated in the upper panels.

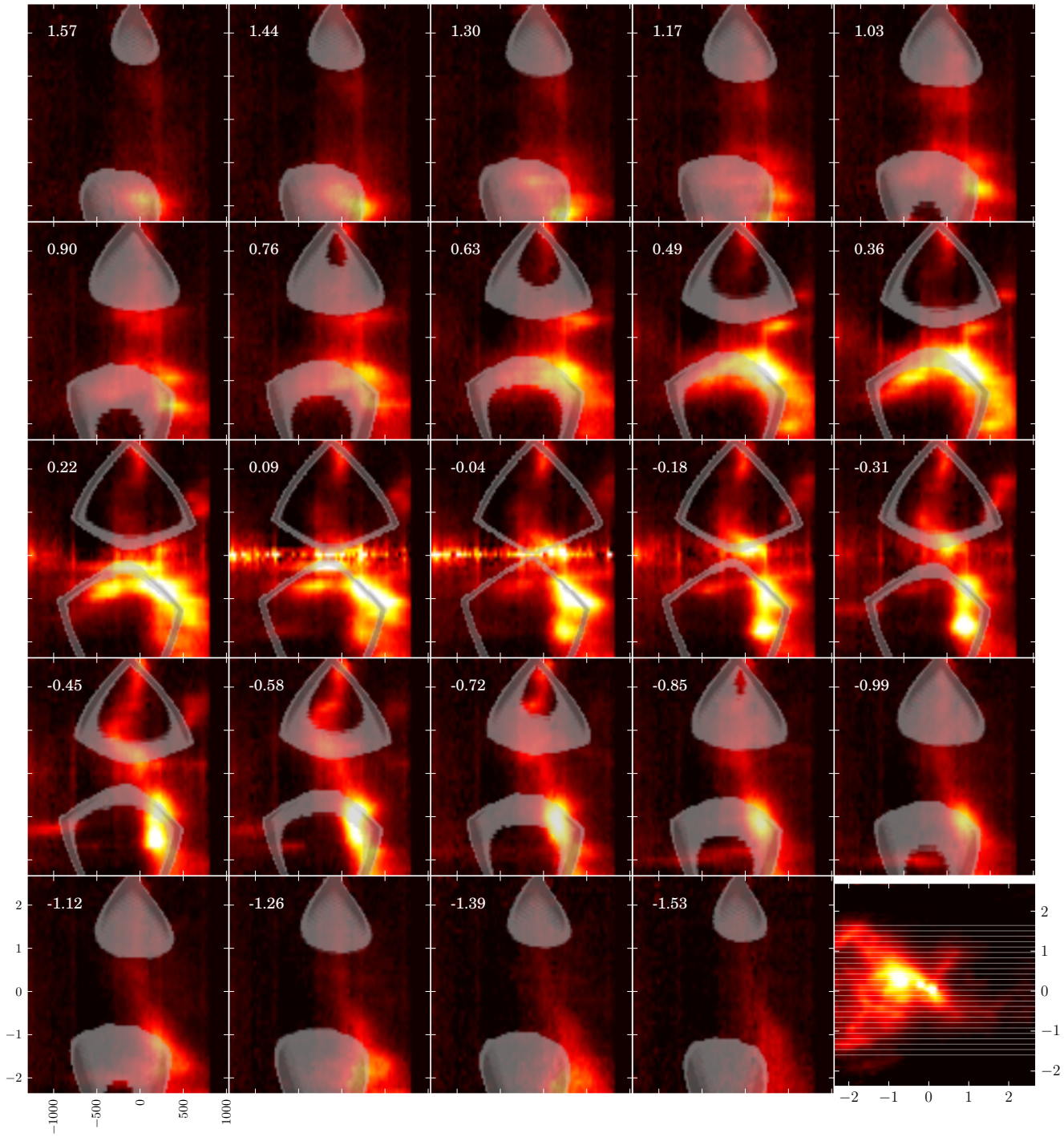


**Figure 16.** Position-velocity diagrams of the accelerated lemniscate outflow model for the [Fe II] line (grey levels) superimposed to data (hot colours). In the lower right panel of the figure we draw the integrated flux map (hot colours) and the lines corresponding to the limits of the adopted slits. The vertical displacement from the nucleus to the center of each slit is displayed in the upper left corner of each panel, in arcsec.

ing gas morphology than the lemniscate model as seen in the integrated flux map (Fig. 11) and in the channel maps (Figure 1 of the Appendix, available online as a supplementary material).

The spherical model fits poorly the data and results in no improvement over the conical model.

The lemniscate model gives a better fit to the flux distribution, but the improvement in the kinematics relative to the conical model is modest: in the $p$-$v$ diagrams, the lemniscate model reproduces better the data for the slits that are farthest away from the centre. In the slits closest to the nucleus, there is a "knee" in the positive velocities at $\approx 1\farcs2$

from the nucleus that is also well reproduced by the lemniscate model. It may be argued that this model shows a narrower range of velocities than the data, particularly noticeable in the central slits of the *p-v* diagrams, but this can be understood as due to the fact that we did not include a velocity dispersion across the walls of the lemniscate. In the conical model, such velocity dispersion arises naturally because of the radial symmetry of the model which leads to a varying orientation of the velocity vectors across the walls of the cone, while, in the same region of the lemniscate model the velocity vectors are parallel.

We would like to point out that, even though the geometric distribution of the gas seems to be better reproduced by the lemniscate model, there is no significant difference between the kinematics of the conical and lemniscate models, both providing similar reproduction of the data. The conical model and the lemniscate model give equally good (or bad!) reproduction of the kinematic data. This is due to the fact that our modeling did not include all the effects present in the data, only a simple geometry and kinematics for the outflow. No velocity component due to gas in the disc was considered in the models, even though they seem to be present in the data. We have also not considered the patchy nature of the outflow, which is obvious in the channel maps, neither the enhanced emission in the redshift channel maps to the NE, as observed in the data. As we have already pointed out, these latter features are due to the interaction between an accretion disc outflow and the circumnuclear ISM of the galaxy. Due to the orientation of the outflow relative to the galaxy plane, the back wall of the NE part of the outflow is tangent to the galaxy plane, encountering much more gas on its way out than the front wall which leaves the plane at a larger angle.

The absence of the effects discussed above in the modelling precludes a quantitative discrimination of the best model to fit the data. As we have stated above we can only say that the lemniscate model gives a somewhat better reproduction of the line flux distributions. An additional discriminator between the models could be obtained if the outflow could be probed at larger distances from the nucleus than we have observed, as the models predict distinct morphologies and behaviors in that regions.

The outflow we are seeing on scales of tens to hundreds of parsecs originates in an accretion disc outflow which occurs on scales 2–3 orders of magnitudes smaller. We are thus observing the interaction of an AGN outflow with the circumnuclear gas at the galaxy. Thus it is remarkable that the observed geometry is so similar to that proposed in accretion disc wind models, such as those of Proga & Kallman (2004) and Proga et al. (2000). The fact that the outflow is hollow supports also an origin in a finite range of radii in the accretion disc as proposed by Elvis (2000). The only difference between the AGN outflow models and the data is the fact that the opening angle of the observed outflow decreases with distance from the nucleus, what seems not to be predicted by the models and may be due to the interaction of the AGN outflow and the circumnuclear gas of the galaxy. It is interesting to note that this feature is observed also in some planetary nebulae (e.g. NGC 6302 and NGC 6537).

## 6 MASS OUTFLOW RATE

In order to quantify the mass outflow rate, consider a cross section of the lemniscate perpendicular to the model axis at a distance of 1 arcsec from the nucleus. This cross section has the geometry of a ring with area $A$. The mass outflow rate is

$$\dot{M}_{out} = m_p \, n_e \, v_{\rm perp} \, f \, A, \tag{4}$$

where $m_p$ is the proton mass, $n_e$ the electron density, $v_{\rm perp}$ is the velocity perpendicular to the cross section and $f$ is the filling factor.

For the velocity $v_{\rm perp}$ we adopt the velocity given by the model at the cross section, 900 km s$^{-1}$, corrected for its orientation relative to the direction perpendicular to the cross section at this location, 40.8°. The result is $v_{\rm perp} = 900 \cos(40.8^\circ) \simeq 680$ km s$^{-1}$.

The filling factor $f$ can be obtained from

$$L_{\rm H\beta} = 4\,\pi\, j_{\rm H\beta}(T)\, V\, f, \tag{5}$$

where $L_{\rm H\beta}$ is the H$\beta$ luminosity emitted by a volume $V$ and $4\,\pi\, j_{\rm H\beta}(T) = (4\,\pi\, j_{\rm H\beta}(T)/n_e\, n_p) \times n_e\, n_p = 1.23 \times 10^{-25} \times 10^4 = 1.23 \times 10^{-21}$ erg cm$^{-3}$ s$^{-1}$ (Osterbrock & Ferland 2006) assuming $n_e = n_p = 10^2$ cm$^{-3}$ and $T = 10000$ K (Case B). Although the temperature and density of the gas are conservative guesses, the value of $4\,\pi\, j_{\rm H\beta}(T)$ for a wide set of possible temperatures and densities ranges from 0.66 to $2.3 \times 10^{-21}$ erg cm$^{-3}$ s$^{-1}$. $L_{\rm H\beta}$ is determined from the flux $F_{\rm Br\gamma}$ using

$$L_{\rm H\beta} = 4\,\pi\, D^2\, F_{\rm H\beta} = 4\,\pi\, D^2\, F_{\rm Br\gamma} \,/\, \frac{j_{\rm Br\gamma}}{j_{\rm H\beta}}, \tag{6}$$

where $D$ is the distance to the galaxy and $j_{\rm Br\gamma}$ and $j_{\rm H\beta}$ are emission coefficients for Br$\gamma$ and H$\beta$, respectively.

The flux $F_{\rm Br\gamma}$ was obtained integrating the Br$\gamma$ flux map over a region with the geometry of a right triangle to the N-NE of the nucleus such that the nucleus is at one of the vertices with angle 50°. This is the angle between the outflow axis (one of the triangle sides) and the wall of the cone model (the triangle hypotenuse). The other triangle side is placed orthogonal to the axis of the outflow at 1 arcsec from the nucleus. This is the region where the Br$\gamma$ is brightest. The integrated flux over this triangular region is $0.534 \times 10^{-15}$ erg cm$^{-2}$ s$^{-1}$. The triangular region over which the flux was integrated corresponds to the projection, in the plane of the sky, of one half of the volume of a cone with the same cross section area of the lemniscate model.

Now dividing equation 5 by 6, solving for $f\,V$ and using that the volume $V$ in equation 5 must be the difference between the volumes of the inner and outer half cones $V = V_o - V_i = \frac{1}{2}\frac{h}{3}\,A_o - \frac{1}{2}\frac{h}{3}\,A_i = \frac{h}{6}(A_o - A_i) = \frac{h}{6}\,A$ we obtain $f\,A$:

$$f\,A = \frac{D^2\; F_{\rm Br\gamma}}{h/6\; j_{\rm Br\gamma}}. \tag{7}$$

Although we are calculating the outflow for a lemniscate geometry and using a conical volume in equations 5 and 6 (the volume is implicit in the integrated flux), this is no mistake as the volume in both equations was the same and its dependence cancel out giving place to a dependence in the area $A$, which is the same as that of the lemniscate model. It is also assumed that the filling factor $f$ is the same for the entire cross section. Inserting 7 in 4 we obtain

$$\dot{M}_{out} = m_p\, n_e\, v_{\rm perp}\, \frac{D^2\ F_{\rm Br\gamma}}{h/6\, j_{\rm Br\gamma}} \quad (8)$$

which does not depend explicitly on geometric details of the outflow.

Now using equation 8 we obtain a mass outflow rate of $\dot{M}_{out} = 1.9\ M_\odot\ {\rm yr}^{-1}$. This value is in agreement with those typical of other active galaxies in Veilleux et al. (2005), which range from 0.1 to 10 $M_\odot\ {\rm yr}^{-1}$ and also with that obtained by Riffel & Storchi-Bergmann (2011b), of 6 $M_\odot\ {\rm yr}^{-1}$, for Mrk 1157 as well as with the revised value for Mrk 1066 (Riffel & Storchi-Bergmann 2011a). As pointed out also in the above studies, such mass outflow rates are much larger than the AGN accretion rate, indicating that, although the origin of the outflow is the AGN, the observed outflow is actually gas from the circumnuclear region being pushed by the AGN outflow ("mass-loaded outflow").

The $\dot{M}_{out}$ value depends mainly on the uncertainties of $v_{\rm perp}$, $D$, $F_{\rm Br\gamma}$ and $j_{\rm Br\gamma}$ and on the assumptions of the modeling. From these parameters the less constrained are the $j_{\rm Br\gamma}$ and $D$. As mentioned above $j_{\rm Br\gamma}$ can span a range from 0.66 to $2.3 \times 10^{-21}$ erg cm$^{-3}$ s$^{-1}$ which corresponds to about $\pm$100% uncertainty. The distance to NGC 1068 $D$ is also very uncertain as in the literature we find values ranging from 10 to 30 Mpc that correspond to an uncertainty of about $^{+100\%}_{-30\%}$. Taking into account these uncertainties, the mass outflow rate is in the range 1 to 4 $M_\odot\ {\rm yr}^{-1}$

We can use the above mass outflow rate to estimate the mechanical power of the outflow using the same method as in Barbosa et al. (2009):

$$P = \frac{1}{2}\, \dot{M}_{out}\, v_{\rm perp}^2. \quad (9)$$

This is a lower limit as this formula does not account for the power associated to the velocity dispersion of the gas, however, this additional term can be neglected as the velocity dispersion is much smaller than the velocity of the outflow. Using the above $v_{\rm perp}$, we obtain $P \cong 2.8 \times 10^{41}$ erg s$^{-1}$, which is in good agreement with those obtained for Seyfert galaxies and compact radio sources (Morganti et al. 2005) and with that found in Riffel & Storchi-Bergmann (2011b), of $P \cong 5.7 \times 10^{41}\,{\rm erg\,s^{-1}}$ for Mrk 1157. The uncertainties for the mechanical power are, in our case, the same as those for $\dot{M}_{out}$ and allow for $P$ values in the range 1.5 to $5.6 \times 10^{41}$ erg s$^{-1}$. Adopting a bolometric luminosity of $L_{Bol} \cong 3.6 \times 10^{44}$ ergs s$^{-1}$ from Pier et al. (1994) (the authors argue that the $L_{Bol}$ is probably within a factor of a few of the published value) for the nuclear source, the mechanical power $P$ is within a factor of a few of 0.08% $L_{Bol}$. The typical power adopted in AGN feedback models to significantly affect the galaxy evolution (e.g. di Matteo et al. 2005) is 0.5% $L_{Bol}$ and, consequently, the outflow mechanical power in NGC 1068 is smaller than that required to provide significant feedback effect in the galaxy. This conclusion depends also on the adopted $L_{Bol}$, as a 7 times smaller value would lead to the opposite conclusion. Woo & Urry (2002) estimated $L_{Bol} \cong 9.55 \times 10^{44}$ and Prieto et al. (2010) calculated $L_{Bol} \cong 8.7 \times 10^{43}$. These values place the limits for our calculated mechanical power in the range 0.03% $L_{Bol}$ to 0.3% $L_{Bol}$. Nonetheless, the values of $L_{Bol}$ for NGC 1068 must be taken as conservative lower limits, as the $A_V$ of the nuclear source is known to be high and this can lead to underestimated values of $L_{Bol}$. These factors lead us to argue that the mechanical power in NGC 1068 is smaller than that required to provide significant feedback effect to the galaxy evolution.

## 7 SUMMARY AND CONCLUSIONS

We have mapped the inner (200 pc) NLR kinematics of the Seyfert 2 galaxy NGC 1068 on the basis of near-IR integral-field spectroscopy in the emission lines [Fe II] $\lambda\,1.644\,\mu$m, $H_2\,\lambda\,2.122\,\mu$m and Br$\gamma$.

We have compared the ionized and molecular gas kinematics and have used three different models to reproduce channel maps and $p$-$v$ diagrams of the ionized gas.

Our main conclusions are:

- The Br$\gamma$ kinematics comprises both blueshifts and redshifts of up to 1000 km s$^{-1}$ and its flux distribution in the channel maps is very similar to the flux distribution in [O III], confirming our conclusion of Paper I that the two originate in the same bi-polar outflow.
- The [Fe II] kinematics cover the same bi-polar outflow and range of velocities as observed for Br$\gamma$, but the flux distributions in the channel maps show a broader (bowl-shaped hourglass) bi-polar morphology than the bi-conical shape previously observed in the [O III] flux distribution and also observed in Br$\gamma$. This is mainly due to the larger contribution of [Fe II] emission in the redshifted channels. We attribute this result to the origin of the [Fe II] emission in a partially ionized region extending beyond the fully ionized region probed by the Br$\gamma$ and [O III] emission, with additional contribution from shocks between the nuclear outflow and gas in the galaxy disk.
- We conclude that the [Fe II] kinematics provide a better coverage of the NLR outflow thus being a better tracer of the outflow than both [O III] and $H^+$ emission lines, as it extends to regions not probed by these lines.
- The bi-polar bowl shape geometry (including the partially ionized gas region) resembles that of many planetary nebulae and that predicted by disc and torus wind models, supporting that such winds are the origin of the observed outflow.
- The $H_2$ kinematics is completely distinct from that of the ionized gas, showing an off-centered ring-like morphology at much lower velocities that suggest expansion in the galaxy plane, at an average velocity of $\approx$100 km s$^{-1}$ as supported by previous CO mm observations.
- A new result regarding $H_2$ is our finding of deceleration between the inner and outer border of the ring from 200 km s$^{-1}$ down to zero, which indicates that the expansion is being halted. This result has been predicted in recent hydrodynamic simulations and can be attributed to the interaction of a nuclear jet with the gas in the galaxy disk. This gas is pushed radially away from the nucleus and subsequently halted by the circumnuclear ISM. This deceleration reconciles our previous finding of a 10 Myr stellar population in the ring with its kinematics.
- Our measurements also suggest that the two $H_2$ linear structures NT and ST (to the north and south of the nucleus) which apparently connect the ring to the galaxy nucleus are in outflow (contrary to the suggested inflows in previous studies).

• We have built models testing three distinct geometries for the outflow observed in [Fe II]: a conical, a spherical and a lemniscate (hourglass). Although the lemniscate model gives a better reproduction of the integrated flux distribution, its kinematics does not provide a significantly better reproduction of the velocity field than the conical model of Das et al. (2006); in both models, the outflow is accelerated to a maximum velocity of 1000 km s$^{-1}$ at 80 pc from the nucleus, decelerating to zero in the conical model and keeping its maximum velocity constant in the lemniscate model for distances larger than 80 pc from the nucleus.

• The calculated mass outflow rate along the NLR is $1.9^{+1.9}_{-0.7}$ M$_\odot$ yr$^{-1}$. Similarly to what we and others have found for other Seyfert galaxies, this outflow rate is much larger than the mass accretion rate to the AGN, indicating that the observed outflow is in fact gas from the inner region of the galaxy pushed by an AGN outflow.

• The calculated power of the outflow is $2.8^{+2.8}_{-1.3} \times 10^{41}$ erg s$^{-1}$, which is only 0.08% $L_{Bol}$, thus smaller than the 0.5% $L_{Bol}$ required to affect significantly the galaxy evolution.

## ACKNOWLEDGMENTS

We thank the referee for valuable suggestions that helped to improve the paper. Based on observations obtained at the Gemini Observatory, which is operated by the Association of Universities for Research in Astronomy, Inc., under a cooperative agreement with the NSF on behalf of the Gemini partnership: the National Science Foundation (United States), the National Research Council (Canada), CONICYT (Chile), the Australian Research Council (Australia), Ministério da Ciência, Tecnologia e Inovação (Brazil) and Ministerio de Ciencia, Tecnología e Innovación Productiva (Argentina).

## REFERENCES

Barbosa, F.K.B., Storchi-Bergmann, T., Cid Fernandes, R., Winge, C., & Schmitt, H., 2009, MNRAS, 396, 2
Cecil, G., Dopita, M. A., Groves, B., Wilson, A. S. & Binette, L., 2002, ApJ 568, 627
Das V., Crenshaw D.M., Kraemer S.B., Deo R.P., 2006, AJ, 132, 620
de Vaucouleurs, G., et al. 1991, Third Reference Catalogue of Bright Galaxies (New York: Springer)
Di Matteo T., Springel V., & Hernquist L., 2005, Nature, 433, 604
Elvis, M. 2000, ApJ, 545, 63
Emsellem, E., Fathi, K., Wozniak, H., Ferruit, P., Mundell, C. G., Schinnerer, E. 2006, MNRAS, 365, 367
Evans, I.N., Ford, H.C., Kinney, A.L., et al., 1991, ApJL, 369, L27
Gerssen, J., Allington-Smith, J., Miller, B. W., Turner, J. E. H., Walker, A., 2006, MNRAS, 365, 29
Gaibler V., Khochfar S., Krause M., & Silk J., 2012, MNRAS, 425, 438
Huchra J.P., Vogeley M.S., Geller M.J, 1999, ApJS, 121, 287
Krips, M., et al., 2011, ApJ, 736, 37
Mazzalay, X., Rodríguez-Ardila, A., Komossa, S. & McGregor, P. J. 2013, MNRAS, 430, 2411
McGregor, P. J. et al., SPIE, 2003, 4841, 1581, eds. Iye, M. & Moorwood, A. F. M.
Morganti R., Tadhunter C.N., & Oosterloo T.A., 2005, A&A, 444, L9
Mouri H., Kawara K, & Taniguchi Y., 2000, ApJ, 528, 186
Müller Sánchez, F., Davies, R.I., Genzel, R., et al. 2009, ApJ, 691, 749
Müller-Sánchez, F., Prieto, M.A., Hicks, E.K.S., et al. 2011, ApJ, 739, 69
Osterbrock, D.E., & Ferland, G.J., 2006, Astrophysics of gaseous nebulae and active galactic nuclei, 2nd. ed. by D.E. Osterbrock and G.J. Ferland. Sausalito, CA: University Science Books, 2006
Pier, E.A., Antonucci, R., Hurt, T., Kriss, G., & Krolik, J., 1994, ApJ, 428, 124
Prieto, M. A., Reunanen, J., Tristram, K. R. W., et al., 2010, MNRAS, 402, 724
Proga, D., Stone, J.M., & Kallman, T.R., 2000, ApJ, 543, 686
Proga, D., & Kallman, T.R., 2004, ApJ, 616, 688
Riffel, Rogemar A. & Storchi-Bergmann, T., 2011, MNRAS, 411, 469
Riffel, R.A. & Storchi-Bergmann, T., 2011, MNRAS, 417, 2752
Riffel, R.A., Storchi-Bergmann, T., & Winge, C., 2013, MNRAS, 430, 2249
Riffel, Rogemar A., Storchi-Bergmann, Vale, T. B., McGregor, P. 2014, MNRAS, in press (Paper I)
Storchi-Bergmann, T., McGregor, P. J., Riffel, R. A., Simões Lopes, R., Beck, T., & Dopita, M., 2009, MNRAS, 394, 1148
Storchi-Bergmann, T., Simões Lopes, R., McGregor, P. Riffel, Rogemar A., Beck, T., Martini, P., 2010, MNRAS, 402, 819
Storchi-Bergmann T., Riffel R.A., Riffel R., et al., 2012, ApJ, 755, 87
Veilleux S., Cecil G., & Bland-Hawthorn J., 2005, ARA&A, 43, 769
Woo, J.-H., & Urry, C. M., 2002, ApJ, 579, 530

This paper has been typeset from a TEX/ LATEX file prepared by the author.